Bioactive Materials 41 (2024) 137–157

Contents lists available at ScienceDirect

Bioactive Materials

journal homepage: www.keaipublishing.com/en/journals/bioactive-materials

STAT3-specific nanocarrier for shRNA/drug dual delivery and tumor synergistic therapy

Le Sun [a,1], Jishang Sun [a,1], Cuiyao Li [a], Keying Wu [a], Zhiyang Gu [a], Lan Guo [a], Yi Zhou [a], Baoqin Han [a,b], Jing Chang [a,b,*]

[a] College of Marine Life Science, Ocean University of China, Qingdao, 266003, PR China
[b] Laboratory for Marine Drugs and Bioproducts, Qingdao Marine Science and Technology Center, Qingdao, 266237, PR China

ARTICLE INFO

Keywords:
Synergistic therapy
Short hairpin RNA
STAT3 signaling pathway
Drug delivery
Tumor treatment

ABSTRACT

Non-small cell lung cancer (NSCLC) is a major disease with high incidence, low survival rate and prone to develop drug resistance to chemotherapy. The mechanism of secondary drug resistance in NSCLC chemotherapy is very complex, and studies have shown that the abnormal activation of STAT3 (Signal Transducer and Activator of Transcription 3) plays an important role in it. In this study, the pGPU6/GFP/Neo STAT3-shRNA recombinant plasmid was constructed with STAT3 as the precise target. By modifying hydrophilic and hydrophobic blocks onto chitosan, a multifunctional vitamin E succinate-chitosan-polyethylene glycol monomethyl ether histidine (VES-CTS-mPEG-His) micelles were synthesized. The micelles could encapsulate hydrophobic drug doxorubicin through self-assembly, and load the recombinant pGPU6/GFP/Neo STAT3-shRNA (pDNA) through positive and negative charges to form dual-loaded nanoparticles DOX/VCPH/pDNA. The co-delivery and synergistic effect of DOX and pDNA could up-regulate the expression of PTEN (Phosphatase and Tensin Homolog), down-regulate the expression of CD31, and induce apoptosis of tumor cells. The results of precision targeted therapy showed that DOX/VCPH/pDNA could significantly down-regulate the expression level of STAT3 protein, further enhancing the efficacy of chemotherapy. Through this study, precision personalized treatment of NSCLC could be effectively achieved, reversing its resistance to chemotherapy drugs, and providing new strategies for the treatment of drug-resistant NSCLC.

1. Introduction

In recent years, lung cancer has become the cancer with the highest morbidity rate, with more than 1.8 million new cases each year, accounting for 13 percent of the total cancer incidence [1]. The lung cancer caused 1.6 million deaths, accounting for 20 percent of the total cancer deaths [2]. Among lung cancer patients, 87 % are non-small-cell lung cancer (NSCLC) patients, and the 5-year survival rate of NSCLC patients is only 15 % [3–5]. Therefore, it is very urgent and important to study the efficient treatment of non-small cell lung cancer [6]. Chemotherapy, as one of the traditional treatment methods for non-small cell lung cancer, has been widely used in clinic. However, the toxic side effects of chemotherapy drugs and the drug resistance generated by tumor cells after a certain course of treatment not only cause great harm to patients, but also greatly reduce the efficacy of drugs [7–9]. The emergence of drug resistance is the stress response of tumor cells against tumor drugs, which is difficult to eliminate completely at present [10].

The mechanisms of secondary drug resistance in patients with NSCLC to chemotherapy drugs are very complex [11]. Currently, several studies have shown that abnormal activation of STAT3 (Signal Transducer and Activator of Transcription 3) plays an important role in this process, representing a new research point for the mechanism of secondary drug resistance in NSCLC [12]. STAT3 is considered the most closely related gene to the occurrence and development of tumors in the STATs family [13,14]. As a transcription factor activated by extracellular signals such as cytokines, growth factors [15] and non-receptor tyrosine kinases [16], STAT3 can act on different DNA segments in the nucleus, regulate the transcription of target genes, and participate in cell growth, invasion, proliferation and differentiation [17,18]. In normal physiology, the activation of STAT3 is brief and rapid, lasting only a few

Peer review under responsibility of KeAi Communications Co., Ltd.
* Corresponding author. Ocean University of China, Qingdao, 266003, PR China.
E-mail address: changjing@ouc.edu.cn (J. Chang).
[1] These two authors contributed equally to this work.

https://doi.org/10.1016/j.bioactmat.2024.07.010
Received 3 April 2024; Received in revised form 28 June 2024; Accepted 5 July 2024

minutes to a few hours. However, studies have shown that STAT3 is persistently activated in almost all solid tumors and hematologic tumors. Excessive activation of STAT3 signaling pathway can mediate drug resistance in tumor cells [19,20]. Blocking the STAT3 signaling pathway with specific or non-specific inhibitors is an effective way to induce apoptosis and reverse drug resistance [21,22].

In the research of targeted therapy for STAT3 signaling pathway, RNA interference (RNAi) technology is gradually developing into an effective tool to specifically inhibit the expression of target genes due to its high efficiency and high specificity [23–25]. The acquisition of high-quality homologous siRNA is a crucial step in RNAi [26]. Currently, methods for preparing siRNA include chemical synthesis [27], *in vitro* transcription [28], Rnase III degraded dsRNA [29], siRNA expression framework [30], and short hairpin RNA (shRNA) expression vector [31]. Due to the lack of self-replication of siRNA prepared *in vitro* in the cell, the concentration of siRNA is greatly reduced under the effects of cell division dilution and chemical degradation, resulting in a short duration within cells and inability to sustain RNAi effects. However, by constructing shRNA expression vectors, shRNA is generated through the enzymatic system of the cells and then converted into siRNA under the action of a series of enzymes [32]. This process avoids direct manipulation of RNA and the degradation effects of Rnase, enabling sustained inhibition of the target gene's expression for several weeks or even longer [33]. Moreover, because the vectors can be easily amplified in large numbers, compared with chemical synthesis, the cost of siRNA preparation can be significantly reduced [34]. Therefore, the utilization of shRNA technology can achieve sustained and efficient inhibition of STAT3 overexpression, effectively overcoming its drug resistance [35].

The synergistic delivery of shRNA with chemotherapeutic drugs is an effective measure to overcome resistance to chemotherapeutic drugs in NSCLC [36]. The main methods of delivering RNA/drugs to tumors include local injection in tumor [37] and systemic administration through the blood system [38]. Local injection into tumor offers precise targeting and can reduce the impact on other tissues and organs, but it is limited by several factors such as the location and size of the tumor [39,40]. Intravenous administration requires stable concentrations of RNA and the drug in the blood, and they must reach and accumulate in the tumor site to enter target cells after circulating through the blood [41]. No matter which delivery method is adopted, there are issues such as toxicity and side effects of chemotherapy drugs, short half-life of RNA, and its susceptibility to degradation by nucleases. These problems can be well solved by selecting suitable carriers to delivery genes and drugs [42–45]. Therefore, efficient gene and drug delivery carriers are key factors influencing delivery efficiency and tumor theatment. Currently, the dual-loaded systems for RNA and antitumor drugs are copolymers of cationic polymers and biodegradable polymers. Liu [46] et al. designed hypoxia-responsive polymeric micelles co-loaded with doxorubicin hydrochloride (DOX·HCl) and shRNA by sequentially targeting tumor hypoxia. The micelles were assembled from methoxy-polyethylene glycol (mPEG) and poly-L-lysine (PLL) copolymers, and azo compound (AZO) acted as a hypoxia-responsive bridge between mPEG and PLL. When exposed to hypoxia, AZO broke down and the micelles decomposed for rapid release. The AZO could deliver drugs and shRNA to the hypoxic site simultaneously and improve the anti-tumor activity of DOX and effectively silencing the HIF-1α pathway. Chen [47] et al. designed an AXL-siRNA (siAXL) loaded glutathione (GSH)-responsive PTX-poly-L-lysine (PTX-PLL; PP) prodrug micelle encapsulated within activated T cell derived exosome delivery system (PP/siAXL@EXO). In tumor cells, exosomal PD-1 attenuated the immunosuppression of the programmed death ligand-1 (PD-L1) and enhanced cellular uptake. siAXL was released to overcome PTX resistance by reversing the epithelial mesenchymal transition (EMT) and inhibiting cellular uptake. The design of this micelle provided a new strategy for the treatment of TNBC.

Chitosan is a typical cationic polymer natural polysaccharide with good biosafety, non-immunogenic, biodegradable and other characteristics [48,49]. The glucosamine group of chitosan can condense genes to form complexes [50]. However, the gene transfection effect using chitosan as carrier alone is not satisfying [51]. In our previous study, we adopted an effective method to modify chitosan by immobilizing basic amino acids onto chitosan as non-viral gene vectors, and found that the histidine modified chitosan could achieve efficient *in vitro* and *in vivo* transfection through proton pump effect [52]. In addition, chemotherapy drugs are usually hydrophobic drugs with large π-conjugated ring structure. In our previous work, we found that by bonding small hydrophobic molecules with π-conjugated ring structure to chitosan polymer chains, the carriers can take advantage of the strong π-π stacking interaction between themselves and antitumor drugs. In this way, the nanoparticles achieved much higher drug load capacity compared to conventional nanoparticles [53,54].

Herein, a novel multifunctional vitamin E succinate-chitosan - polyethylene glycol monomethyl ether - histidine (VES-CTS-mPEG-His) micellar was synthesized by modifying chitosan with hydrophilic and hydrophobic block. This micelle can encapsulate the hydrophobic drug doxorubicin (DOX) through self-assembly and bind to the recombinant plasmid pGPU6/GFP/Neo STAT3-shRNA (pDNA) through electrostatic interaction, forming DOX/VCPH/pDNA composite nanoparticles that load both drugs and genes (Scheme 1). The π-π stacking interaction between VES and DOX is utilized to increase the drug loading capacity. Meanwhile, the histidine-modified chitosan on the hydrophilic shell of the nanoparticles is loaded with shRNA targeting STAT3 gene silencing, achieving efficient transfection of NSCLC cells, downregulating the expression level of STAT3 protein, and eliminating the drug resistance of NSCLC. Both *in vivo* and *in vitro* results demonstrated that the synergistic effect of genes and drugs could significantly enhance the therapeutic effect of chemotherapy drugs on NSCLC. The implementation of this study will obtain a new type of gene/drug dual-loaded system, which will provide new ideas and methods for the treatment of drug-resistant NSCLC and promote the development of cancer treatment research.

2. Materials and methods

2.1. Materials

Chitosan (M_W = 20 KD, DD > 90 %) was purchased from Qingdao Biotemed Biomaterial Co., Ltd (Qingdao, China). Polyethylene glycol monomethyl ether (mPEG, Mw = 2000 D) was purchased from Shanghai Yayi Biotechnology Co., LTD. Vitamin E succinate (D-α-tocopherol succinate) and PEI 25 K were purchased from Sigma-Aldrich chemicals Pvt., Ltd. Fluorescein isothiocyanate (FITC) and Cy5 were purchased from Beijing Solaibao Technology Co., LTD. Doxorubicin hydrochloride (DOX·HCl) was obtained from Meilun Biotechnology Co., Ltd (Dalian, China). 1-ethyl-3-[3-(dimethylamino) propyl] carbodiimide (EDC·HCl) and N-Hydroxy succinimide (NHS) were purchased from Solarbio Science & Technology Co., Ltd (Beijing, China). DC202 Plasmid Extraction Kit were purchased from Nanjing Nuoweizan Biotechnology Co., LTD. Dulvecco's modified Eagle's medium (DMEM) were purchased from Hyclone Inc. Ham's F–12K nutrient medium were purchased from Gibco Inc. MTT (3-(4,5-dimethylthiazol-2-yl)-2,5-diphenyltetrazolium bromide) was purchased from Sigma-Aldrich (St. Louis, MO, USA). All the solvents were obtained from Huasheng Reagent Co., Ltd. (Qingdao, China) and purified before used. The human non-small cell lung cancer cells A549 and mouse fibroblast cells L929 were supplied by Cell Bank of Chinese Academy of Sciences. BALB/c female nude mice weighing 20 ± 2 g were supplied by the Spife Biotechnology Co., LTD. All animals were kept under a 12 h light-dark cycles at consistent temperature (25 ± 3 °C) and relative humidity (60–70 %). Experiments were performed in accordance with the ethical guidelines of the Experimental Animal Management Committee of Ocean University of China and were in complete compliance with the National Institutes of Health Guide for the Care and Use of Laboratory Animals.

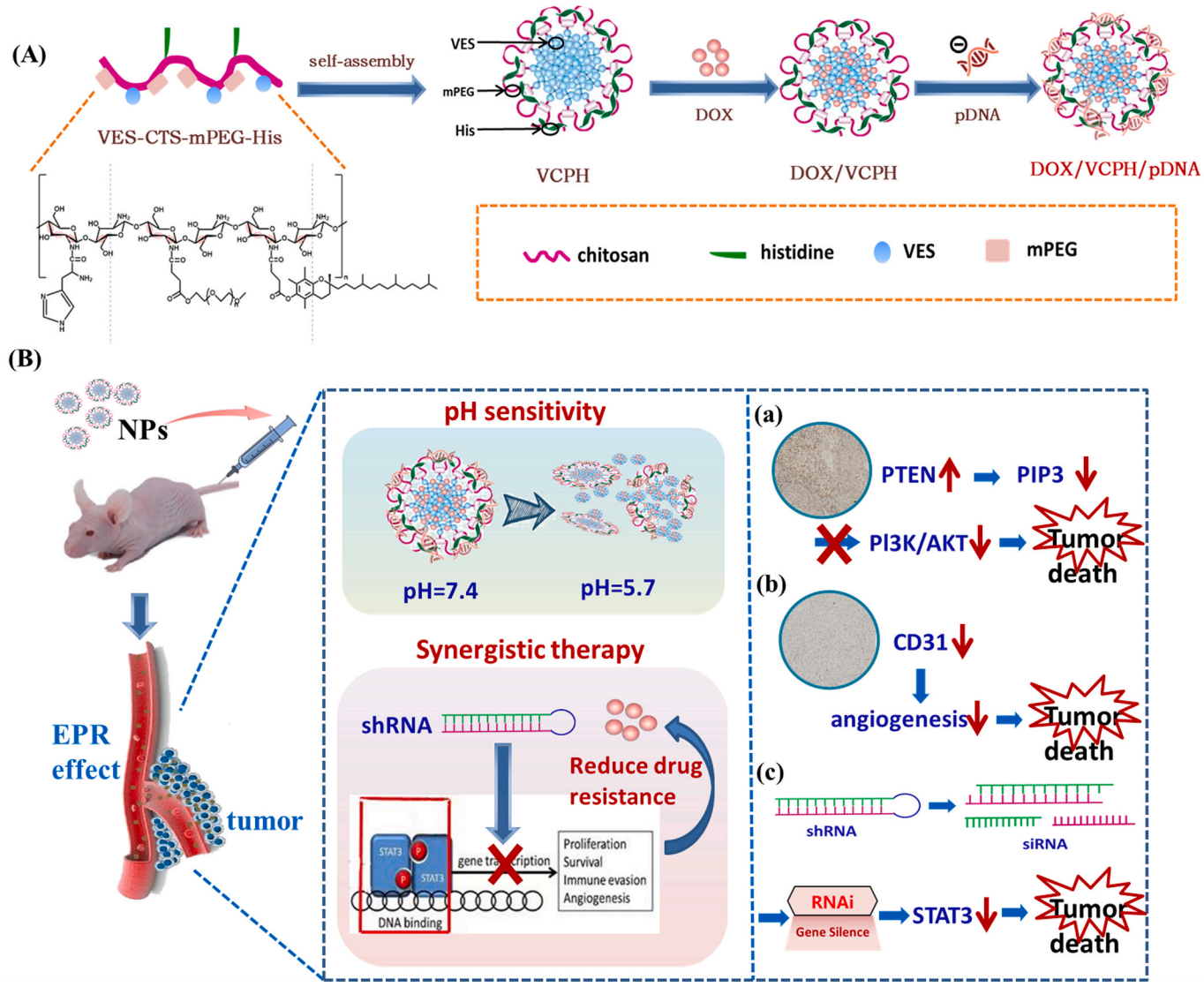

Scheme 1. (A) The structure and assembly of VCPH nanoparticles. (B) The mechanism of VCPH nanoparticles.

2.2. Synthesis of vitamin E succinate - chitosan - polyethylene glycol - histidine (VCPH)

The synthesis scheme for the VCPH was shown in Fig. 1. In brief, the VES (1.59 g) was dissolved in N,N-dimethylformamide (DMF) (120 mL) with the addition of EDC·HCl (1.15 g) and NHS (0.69 g) to activate the carboxylic acid groups for 2 h. The low molecular chitosan (0.24 g) was dissolved in 60 mL 0.5 % hydrochloric acid solution. The dissolved chitosan solution was then added into the activated VES solution dropwise under vigorous stirring, and the mixture was stirred for 48 h at the ambient temperature in darkness. The reaction solution was precipitated by anhydrous ethanol for several times and placed in dialysis bags with an interception rate of 8000–14000 k for dialysis. VES-CS (VC) was obtained by lyophilization. Then the VC (0.24 g) was dissolved in 60 mL 0.5 % acetic acid solution by stirring. The mPEG (0.2 g) was dissolved in 60 mL 0.5 % acetic acid, with 0.57 g EDC and 0.34 g NHS added and stirred for 2 h. VC solution was added dropwise and reacted for 36 h. The reaction solution was put into dialysis bag with interception rate of 3500 k for dialysis. The VES–CS–mPEG (VCP) sample was obtained by lyophilization. Finally, the VCP (0.4 g) was dissolved in 80 mL 0.5 % acetic acid. The histidine (0.193 g) was dissolve in ddH_2O, with 0.286 g NHS and 0.476 g EDC·HCl stirred for 2 h. The VCP solution was added drop by drop into the mixture and react for 24 h. The reaction solution was placed in dialysis bags with an interception rate of 8000–14000 k for dialysis, and lyophilized to obtain the VCPH.

2.3. Characterization of VCPH

The characterization of the products was analyzed by ^{1}H NMR and FT-IR. The ^{1}H NMR spectrum (400 MHz) was recorded using an Agilent 500 MHz spectrometer. The FT-IR spectrum was obtained on a Thermo Scientific Nicolet Nexus-470 in transmittance mode in the range of 4000–400 cm^{-1}. The VCPH was dissolved in pH 7.4 PBS buffer and acetic acid, respectively. After ultrasonic treated, the mean size, size distribution and zeta potential of the VCPH were measured by a Malvern Zetasizer 2000 (Malvern, UK). The morphology of the VCPH was examined by Scanning Electron Microscopy (SEM, Hitachi S4800). The VCPH was dissolved in deionized water and an aqueous solution of VCPH was dropped onto a clean mica sheet and dried before SEM measurement. All measurements were done at room temperature and the data were obtained in triplicate.

2.4. Stability of VCPH nanoparticles under physiological conditions

The VCPH was dissolved in PBS buffer (pH = 7.4) with a concentration of 1 mg/mL. After sonication, the mean sizes, size distribution

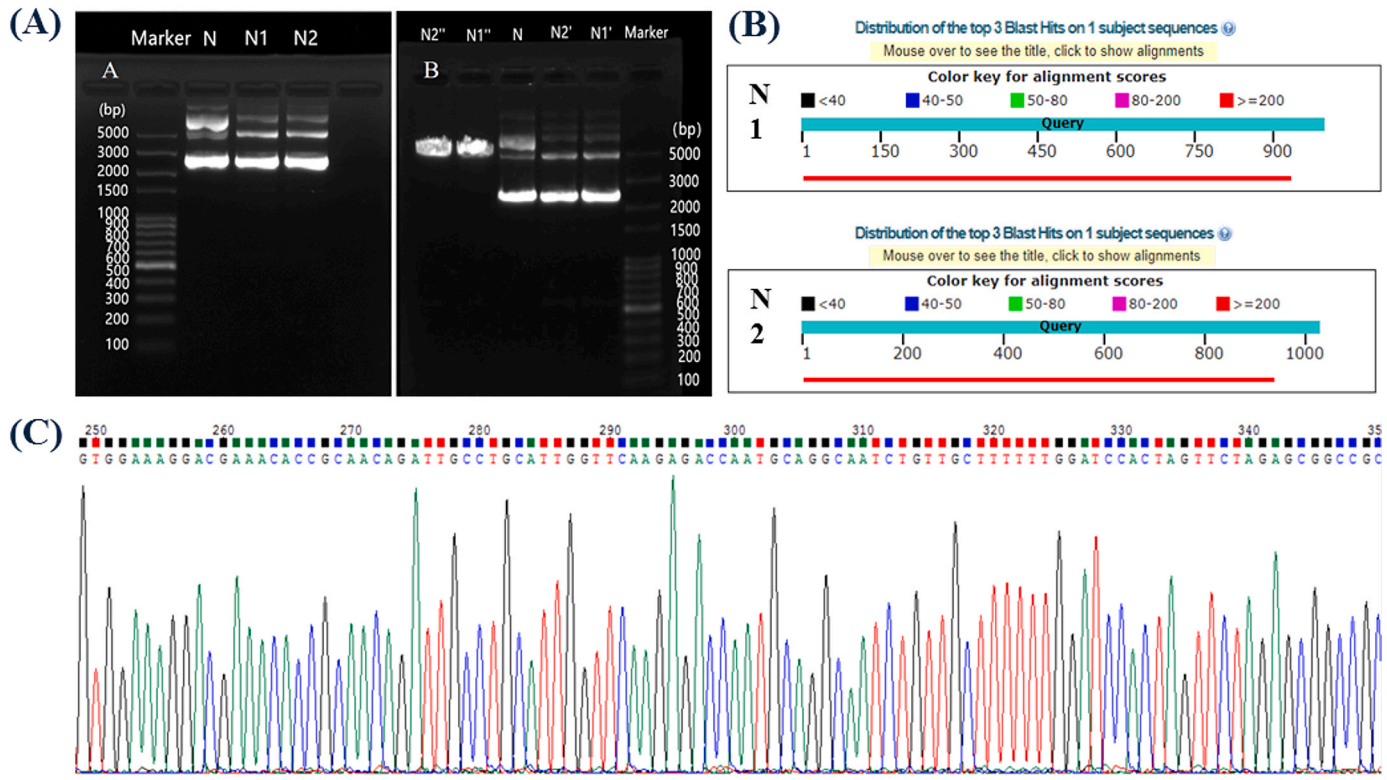

Fig. 1. (A) Preliminary electrophoresis analysis of recombinant plasmid and restriction electrophoresis analysis. N: pGPU6/GFP/Neo STAT3-shRNA recombinant plasmid; N1&N2: amplification plasmid; N1'&N2': Pst I restriction; N1''&N2'': BamH I restriction. (B) Sequence comparison image of pGPU6/GFP/Neo STAT3-shRNA amplification plasmids. (C) Sequencing result of pGPU6/GFP/Neo STAT3-shRNA amplification plasmids.

and zeta potentials of the VCPH were measured on 0, 1, 3, 5 and 7 days by a Malvern Zetasizer 2000 (Malvern, UK).

2.5. Preparation and characterization of drug loaded micelles (DOX/VCPH)

DOX-loaded VCPH NPs were prepared by a nanoprecipitation method using a DMSO/water system. Briefly, 100 mg VCPH was dissolved in 100 mL deionized water and the DOX powder was dissolved in 10 mL DMSO (the weight ratio of VCPH to DOX was varied from 2:5 to 4:5). The two solutions were mildly blended and stirred at 4 °C for 12 h in the dark, followed by ultrasonic treatment in ice bath. The mixture was transferred to a dialysis bag (MWCO = 2000) and dialyzed against deionized water at 4 °C for 12 h. The solution in the dialysis bag was then centrifuged and subsequently lyophilized to obtain DOX/VCPH solution. The zeta potential and size of the micelles was evaluated by Dynamic Light Scattering (DLS, Malvern Zetasizer Nano ZS) and Scanning Electron Microscopy (SEM, Hitachi S4800). The interaction between the VCPH and DOX was explored using UV–vis absorption. The content of DOX was determined by ultraviolet–visible spectrophotometer at 485 nm in DMSO using calibration curve obtained from DOX/DMSO solutions with different DOX concentrations. Drug loading content (DLC) and encapsulation efficiency (EE) were calculated *via* the following formula:

$$\mathrm{DLC}(\%) = \frac{\text{weight of the DOX micelles}}{\text{weight of the feeding polymer and DOX}} \times 100\% \quad (1)$$

$$\mathrm{EE}(\%) = \frac{\text{weight of the DOX micelles}}{\text{weight of the feeding DOX}} \times 100\% \quad (2)$$

2.6. Construction and extraction of pGPU6/GFP/Neo STAT3-shRNA (pDNA)

STAT3-targeting and negative-control shRNAs were sourced by Gene Pharm Technologies (Shanghai, China). The sequences of STAT3-targeting and negative-control shRNAs were shown in Table 1. Stable culture of *E. coli* DH5α was transformed with the plasmids (pGPU6/GFP/Neo STAT3-shRNA) that encoded shRNA and targeted the mRNA of STAT3, and the plasmids (pGPU6/GFP/Neo scramble-shRNA) were obtained using the same method.

2.7. The particle sizes, zeta potentials and SEM images of DOX/VCPH/pDNA with different N/P ratios

DOX/VCPH and pDNA were mixed according to different N/P ratios of 35, 45, 55 and 65. The mixtures were incubated for 2 h at 37 °C. After sonication, the mean sizes, size distribution and zeta potentials of the DOX/VCPH/pDNA with different N/P ratios were measured by a Malvern Zetasizer 2000 (Malvern, UK). The morphology was examined by Scanning Electron Microscopy (SEM, TESCAN VEGA3). All measurements were done at room temperature and the data were obtained in triplicate.

2.8. Preparation and characterization of DOX/VCPH/pDNA

DOX/VCPH solution was prepared with the optimal ratio of DOX and VCPH, and then the pDNA solution was added into DOX/VCPH solution with N/P ratio of 55. The solution was fully mixed and left for half an hour at 37 °C, the stable DOX/VCPH/pDNA composite particles could be prepared by electrostatic action. Polyethylenimine (PEI) was combined with recombinant plasmid pDNA (N/P = 10) to prepare PEI/pDNA nanoparticle, which was used as the positive control. The zeta potential and size of the DOX/VCPH/pDNA was evaluated by Dynamic Light

Table 1
The sequences of STAT3-shRNA and scramble-shRNA.

Samples	Sequences
STAT3-shRNA sense strand	5′-GATCCAAAAAAGCAACAGATTGCCTGCATTGGTCTCTTGAACCAATGCAGGCAATCTGTTGC-3′
STAT3-shRNA antisense strand	5′-GATCCAAAAAAGCAACAGATTGCCTGCATTGGTCTCTTGAACCAATGCAGGCAATCTGTTGC-3′
scramble-shRNA sense strand	5′-CACCGTTCTCCGAACGTGTCACGTCAAGAGATTACGTGACACGTTCGGAGAATTTTTTG-3′
scramble-shRNA antisense strand	5′-GATCCAAAAAATTCTCCGAACGTGTCACGTAATCTCTTGACGTGACACGTTCGGAGAAC-3′

Scattering (DLS, Malvern Zetasizer Nano ZS) and Scanning Electron Microscopy (SEM, Hitachi S4800).

2.9. In vitro drug release study of DOX/VCPH

To evaluate the drug release behaviors, a fixed amount of DOX-loaded VCPH micelles was suspended in 1 mL PBS solutions and the dialysis bags (mw: 8000–14000) in 25 mL PBS buffer of different pH values (pH = 5.7 and pH = 7.4) were used at 37 °C to separate the DOX and the VCPH. At each time interval, the buffer solution outside the dialysis bag was collected for UV–vis spectrophotometer at 485 nm. According to the doxorubicin standard curve, the cumulative release of doxorubicin was calculated as follows:

$$\text{Cumulative Release}(\%) = \frac{\text{DOX weight in buffer solution}}{\text{total DOX weight in each sample}} \times 100\% \quad (3)$$

2.10. pH sensitivity of VCPH and DOX/VCPH nanoparticles

The VCPH and DOX/VCPH was dissolved in different PBS buffers (pH = 7.4 and pH = 5.7) with a concentration of 1 mg/mL. After sonication, the mean sizes, size distribution and zeta potentials of the VCPH were measured by a Malvern Zetasizer 2000 (Malvern, UK). The morphology of DOX/VCPH was observed using transmission electron microscopy (TEM, JEOL JEM-1400 flash) and Scanning Electron Microscopy (SEM, TESCAN VEGA3).

2.11. The cytotoxicity assay of VCPH

The cytotoxicity of the VCPH nanoparticles was assessed using a MTT [3-(4,5-dimethyl-2-tetrazolyl)-2,5-diphenyl-2H-tetrazolium bromide] assay. In brief, the L929 cells were centrifuged and diluted to a density of 2×10^4 cells/mL, which were cultured in 96-well plates for 24 h. The medium containing different concentrations of VCPH nanoparticles (10, 50, 100, 200 μg/mL) was added into the wells. The normal cultured cells without VCPH nanoparticles were set as control group, and the wells without cells were set as blank group. After the treatments of 24 and 48 h, the morphology of the cells was recorded by invert microscope (T1-SM100, Nicon, Japan). Then each well was added with 20 μL MTT solution, incubated for 4 h in darkness, and then each well was added with 150 μL DMSO solution. After incubation for 10 min at 37 °C, the absorbance of each well was measured at 492 nm in the microplate reader (Multiskan Go, Thermo Fisher Scientific, USA). The relative cell proliferation rate at 24 h and 48 h was calculated according to the following formula. The cytotoxicity assay of VCPH on A549 cells were carried out by the same method.

$$\text{Cell Viability}(\%) = \frac{\text{Absorbance of cells exposed to the sample} - \text{Absorbance of blank group}}{\text{Absorbance of untreated cells} - \text{Absorbance of blank group}} \quad (4)$$

2.12. Hemolytic tests of VCPH, DOX/VCPH, VCPH/pDNA and DOX/VCPH/pDNA

The fresh blood was collected into blood collection tubes directly via KM mice. After shaking fully, the blood cells were obtained by centrifugation at 2500 rpm for 15 min and the precipitate was added into normal saline solution. After washing and centrifuge several times, the red blood cell suspension with a concentration of 2 % was obtained. The VCPH were dissolved in normal saline at different concentrations of 10, 50, 100 and 200 μg/mL. The blood cell solution was mixed with different concentrations of VCPH solution in a 1:1 vol ratio. The normal saline was used as negative control and the distilled water was used as positive control. After incubating for 2 h at 37 °C, the mixed solution was centrifuged at 3000 rpm for 15 min and photographed. The value of absorbance of supernatant was measured at 542 nm using a microplate reader (Multiskan Go, Thermo Fisher Scientific, USA). The Hemolytic tests of DOX/VCPH, VCPH/pDNA and DOX/VCPH/pDNA were studied by the same method. Hemolytic rate was calculated according to the following formulas:

$$\textit{Hemolytic Rate}\ (\%) = \frac{A_t - A_n}{A_p - A_n} \times 100\% \quad (5)$$

Where A_t referred to the absorbance of the given concentrations samples, where A_n referred to the absorbance of negative control concentrations, where A_p referred to the absorbance of positive control concentrations.

2.13. In vitro antitumor efficacy of DOX/VCPH/pDNA

A549 cells in logarithmic growth phase were planted in 96-well plates at a concentration of 2×10^4 cells/mL, with cell suspension of 200 μL per well. After incubating for 24 h, the medium was discarded and 200 μL fresh medium containing DOX·HCl, DOX/VCPH or DOX/VCPH/pDNA (the final concentration of DOX in the medium ranged from 0.1 to 100 μg/mL) was added. After incubation for another 24 h, 20 μL MTT solution was added to each well, and then the cells were incubated in a cell incubator for 4 h. The medium was discarded and 150 μL DMSO was added, then the cells were incubated in a microplate apparatus at 37 °C for 10 min. The absorbance value of each well was detected at 492 nm wavelength, and the relative proliferation rate of cells was calculated. The relative cell proliferation rate was calculated according to the following formula:

$$\text{Cell Viability}\ (\%) = \frac{\text{Absorbance of cells exposed to the sample} - \text{Absorbance of blank group}}{\text{Absorbance of untreated cells} - \text{Absorbance of blank group}} \times 100\% \quad (6)$$

2.14. Calcein/PI staining of A549 cells with different nanoparticles

A549 cells in logarithmic growth phase were planted in 96-well plates at a concentration of 2×10^4 cells/mL, with cell suspension of 200 μL per well. After incubating for 24 h, the medium was discarded and 200 μL fresh medium containing DOX·HCl, DOX/VCPH, VCPH/pDNA, DOX/VCPH/pDNA, PEI/pDNA (the final concentration of DOX in the medium was 20 μg/mL) was added. After incubation for another 24 h, the medium was discarded and 200 μL PBS was added. After rinsed three times with PBS buffer (0.01 M, pH 7.4), 100 μL Calcein/PI stain was added to each well under dark condition, and the results were obtained using a fluorescence microscope (Leica, Germany) after incubation for 30 min.

2.15. Flow cytometry of A549 cells with different nanoparticles

A549 cells in logarithmic growth phase were planted in 6-well plates at a concentration of 1.5×10^5 cells/mL, with cell suspension of 2 mL per well. After incubating for 24 h, the medium was discarded and 2 mL fresh medium containing DOX·HCl, DOX/VCPH, VCPH/pDNA, DOX/VCPH/pDNA, PEI/pDNA (the final concentration of DOX in the medium was 20 μg/mL) was added. After incubation for another 24 h, the cells were collected, stained with Annexin V-FITC/PI apoptosis detection kit, and then detected by flow cytometry.

2.16. In vitro gene transfection efficiency of DOX/VCPH/pDNA

The gene transfection efficiency of the VCPH was evaluated with A549 cells. The VCPH/pDNA and DOX/VCPH/pDNA complexes were obtained at the N/P ratio of 55. The A549 cells were added to 24-well plates (10^5 cells per well) and then cultured under an atmosphere of 5 % CO_2 for 24 h. The VCPH/pDNA and DOX/VCPH/pDNA complexes containing 0.8 μg pDNA were added to 24-well plates in DMEM without FBS. After 4 h of cultivation, the complexes were removed and replaced with fresh DMEM, after which the well plates were incubated at 37 °C for another 48 h. The results were obtained using a fluorescence microscope (Leica, Germany) and by using the flow cytometry method (FACE Vantage, BD, USA). The transfected A549 cells with naked pDNA and the transfected A549 cells with PEI 25 K served as negative and positive controls, respectively.

2.17. Cellular uptake of DOX/VCPH/pDNA

A549 cells in logarithmic growth phase were seeded in glass cell culture dishes with diameters of 35 mm at a density of 2×10^4 cells per well. After incubating for 24 h, the culture medium was removed and the cells were incubated with the medium containing DOX·HCl and DOX loaded FITC-labeled nanoparticles (DOX concentration of 10 μg/mL). After culture for 1 h, 3 h and 5 h, the original culture medium was removed, and Hoechst 33258 staining solution was added to stain for 10 min. Then the cells were washed with PBS buffer (0.01 M, pH 7.4) for three times. Intracellular fluorescence was observed and photographed under a confocal scanning laser microscope (CLSM, JM0L JSM-840). The excitation wavelength of DOX was 485 nm and the emission wavelength was 595 nm. The excitation wavelength of Hoechst33258 was 352 nm and the emission wavelength was 461 nm. The excitation wavelength of FITC was 495 nm and the emission wavelength was 525 nm.

2.18. In vivo antitumor activity study of DOX/VCPH/pDNA

A549 cells in logarithmic growth phase were obtained by ascites culture. A549 cells were injected into the right axilla subcutaneously of female BALB/c nude mice at the concentration of 1×10^7 cells/mL, and 0.1 mL cell suspension was injected into each mouse. Tumor model was successfully established when the inoculated tumor volume came to 80–100 mm^3. And then the mice were randomly divided into six groups (normal saline group, DOX·HCl group, DOX/VCPH group, DOX/VCPH/pDNA group, VCPH/pDNA group and PEI/pDNA group). Each group was injected *via* the tail vein at a dose of 5 mg DOX per kg at a 3 days interval, normal saline group was injected equivalent dose. After four times treatment, all mice were sacrificed and then the heart, liver, lung, spleen, kidney as well as tumor tissues were taken out, washed with normal saline, weighed and fixed in 4 % formaldehyde. Then they were paraffin embedded, sliced and staining for histological and immunohistochemical analysis.

The size of tumor volume was calculated according to the following formula:

$$V_{Tumor} = \frac{L \times W^2}{2} \quad (6)$$

Where V_{Tumor} referred to the tumor volume, L referred to the tumor length, and W referred to the tumor width.

The visceral index was calculated using the following equation:

$$\text{Visceral Index} = \frac{W_V}{W_B} \times 100\% \quad (7)$$

Where W_V referred to the weight of heart, liver, spleen, lung, kidney and other organs of mice, W_B referred to the average weight of mice.

The tumor inhibition radio was calculated using the following equation:

$$TIR = \left(1 - \frac{W_T}{W_C}\right) \times 100\% \quad (8)$$

Where W_T referred to the average tumor weight of the experimental group, and W_C referred to the average tumor weight of the control group.

2.19. Real-time PCR of STAT3

The total RNA of the tumor tissues was extracted with Trizol (Takara, Dalian, China) following the manufacturer's protocol. The reverse transcription was achieved using the Prime Script RT reagent kit (Takara). The primers used for STAT3 and the β-actin gene were as follows: STAT3 forward, 5′-GCTA CAGCAGCTTGACACACG-3′ and STAT3 reverse, 5′-G TGGCATGTGATTCTTTGCTGGC-3'; β-actin forward, 5′- AGAAAATCTGGCACCACACC-3′ and β-actin reverse, 5′-TAGCACAGCCTGGATAGCAA-3'. β-actin was used as an endogenous control. The PCR set cycle conditions were 98 °C for 5 min, 98 °C 10 s, 50 °C for 15 s, 72 °C for 30 s, after which the relative STAT3 expression was estimated by qRT-PCR (Roche, Germany) and obtained based on the 2-ΔΔCt method (Schmittgen and Livak, 2008).

2.20. Western blotting of STAT3

The proteins of tumor tissues were extracted with RIPA buffer. The different samples were assessed by sodium dodecyl sulfate-

polyacrylamide gel electrophoresis (SDS-PAGE). Then, the membranes were incubated with different antibodies. The antibodies used were as follows: rabbit anti-human STAT3 (1:600), mouse anti-human β-actin (1:200), goat anti-rabbit 1gG-HRP (1:1000), and goat anti-mouse 1gG-HRP (1:1000). At last, the protein bands were visualized using DBA (Lunavat et al., 2016), and the bands were analyzed by the Image J software.

2.21. Statistical analysis

All data were expressed as means ± SD of a representative of several similar experiments. Statistical difference between several groups was evaluated *via* a one-way analysis of variance (ANOVA), and a value of $P < 0.05$ was considered significant (computed by SPSS version 13.0 Software).

3. Results and discussion

3.1. Construction and sequence analysis of recombinant plasmid

Two endonuclease enzymes, BamH I and Pst I, were used to identify the amplified plasmid. The recombinant plasmid could be digested by BamH I enzyme because it contained BamH I enzyme cleavage site, while Pst I had no effect on the recombinant plasmid. As shown in Fig. 1 (A), N was the electrophoretic band of recombinant plasmid. N1' and N2' were the electrophoretic band of amplified plasmid digested by Pst I, and the lane contained ring plasmid and notch plasmid bands. N1" and N2" were the electrophoretic band of amplified plasmid digested by BamH I, and the lane contained only one line plasmid electrophoresis band digested by enzyme. The recombinant plasmid was successfully amplified. After enzyme digestion identification, gene sequencing was performed on the amplified plasmid (Fig. 1 (C)), and the results were shown in Fig. 1 (B). Comparing the amplified plasmid sequence with the targeted STAT3 sequence, it was found that the base sequences of the two were basically consistent, which proved that the recombinant plasmid was successfully amplified.

3.2. Structural characterization of VC, VCP and VCPH

Fig. 2 (A) showed the synthesis of VES-CTs-mPEG-His (VCPH) by grafting vitamin E succinate (VES), polyethylene glycol monomethyl ether (mPEG) and histidine (His), respectively. The reaction was achieved by the formation of amide bonds under the activation catalysis of NHS and EDC·HCl. Fig. 2 (B) showed the infrared spectra of CTS, VC, VCP and VCPH. The band at 2923 cm^{-1} was the antisymmetric stretching vibration peak of alkane-CH_2, the absorption peak at 1717 cm^{-1} was the C═O stretching vibration peak of VC, and the absorption peak at 2872 cm^{-1} was the –CH_2-symmetric stretching vibration peak of mPEG. The absorption peak of 1106 cm^{-1} was the -C-O-C-symmetric stretching vibration peak of mPEG, the absorption peak of 1559 cm^{-1} was the N–H bending vibration peak of secondary amide, and the C═N vibration absorption peak of imidazole ring. The absorption peak of 1094 cm^{-1} was the bending vibration peak of –CCN on imidazole ring. The results showed that the vitamin E succinate, polyethylene glycol monomethyl ether and histidine were successfully grafted onto the amino group of chitosan.

Fig. 2 (C) was the ^1H NMR spectra of the intermediate products VC, VCP and the end product VCPH. It could be seen from the figure that the proton peaks at 0.61 and 1.01 ppm belonged to the hydrogen (H_1, H_3 and H_5) signal peaks of methyl and methylene in long straight alkyl on vitamin E succinate. The proton peak at 1.85 ppm was attributed to the hydrogen (H_2) signal peak on the benzofuran-6 ring of vitamin E

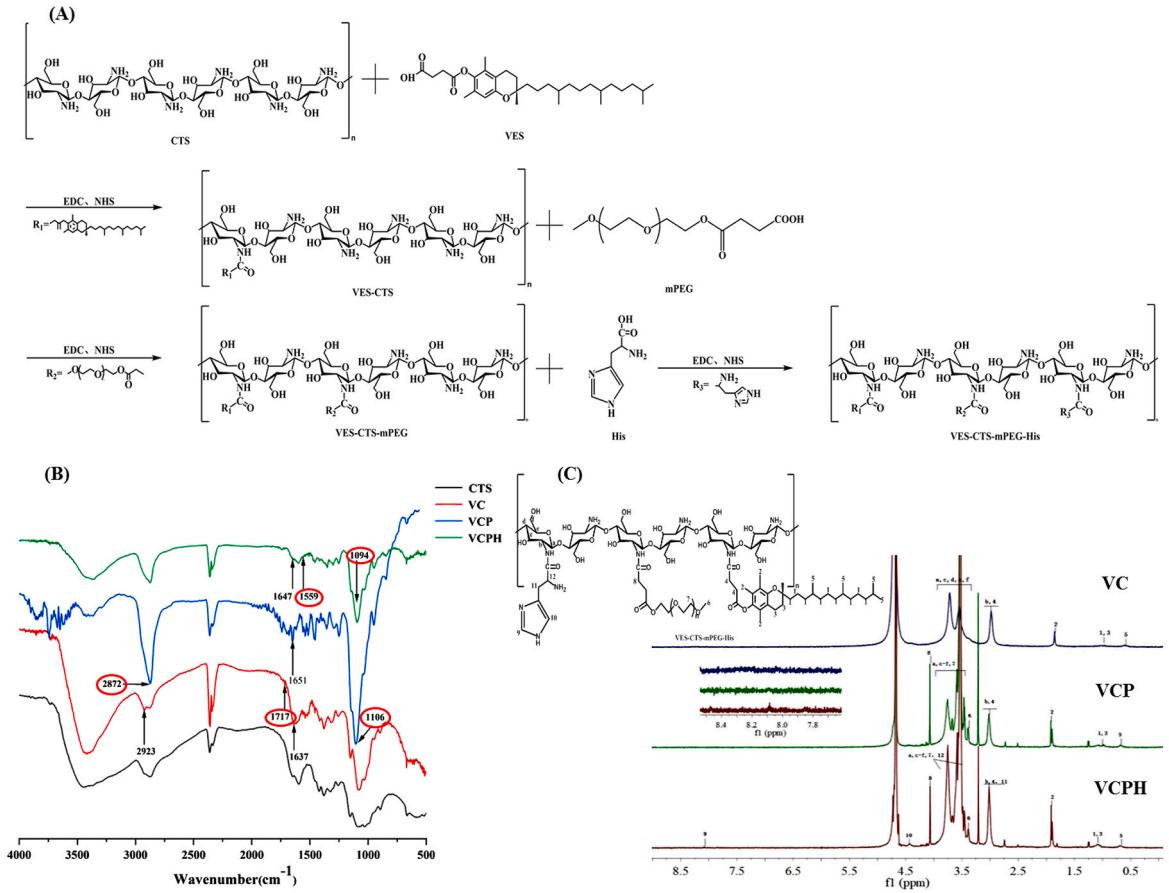

Fig. 2. Schematic diagram of the preparation of the amphiphilic self-assembled polymer VCPH (A). The FTIR spectra (B) and the ^1H NMR spectra (C) of VCPH.

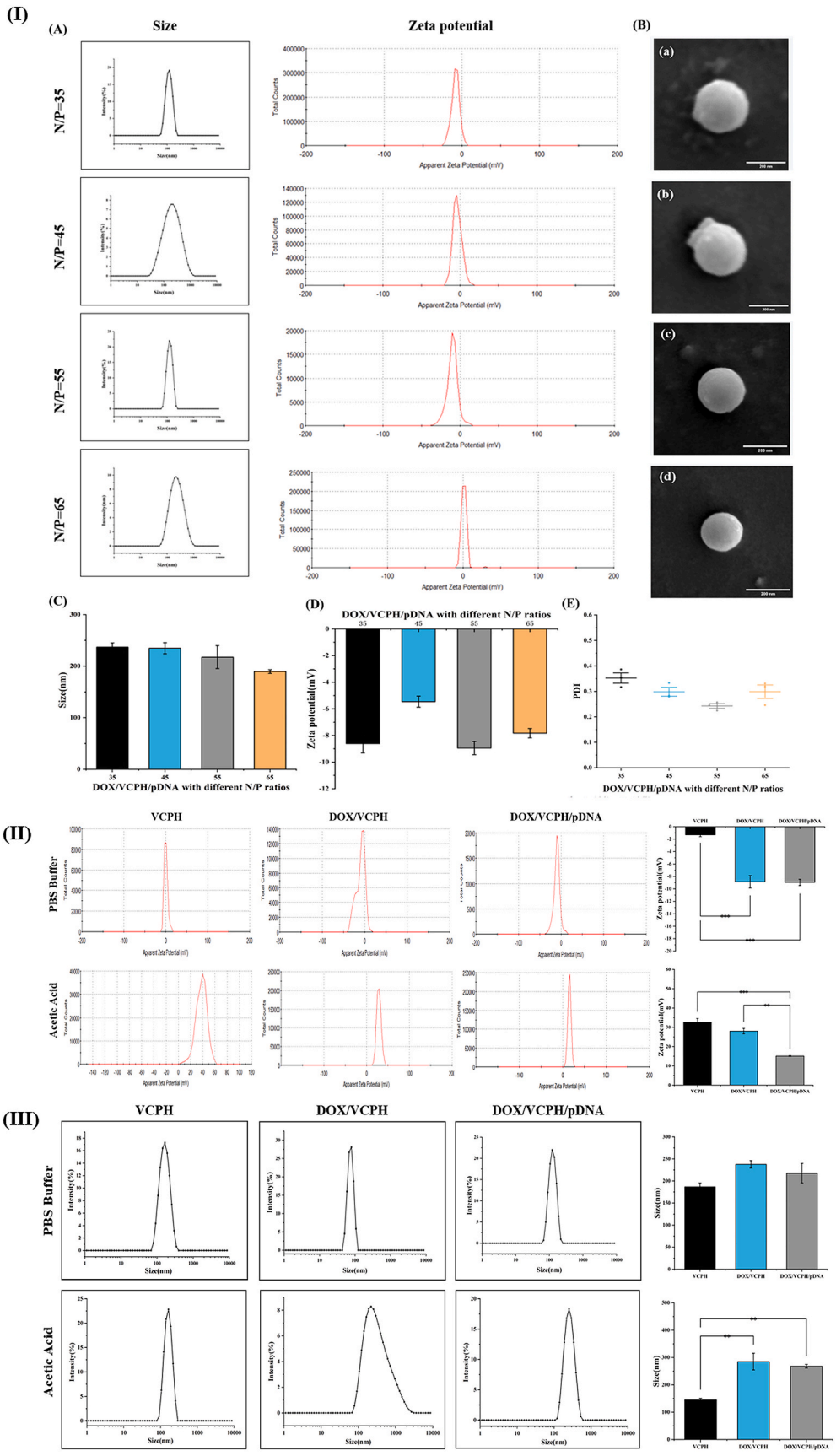

Fig. 3. (I) The effect of different N/P ratios on characteristic of nanoparticles. (A) The particle sizes and zeta potentials of DOX/VCPH/pDNA with different N/P ratios. (B) SEM images of DOX/VCPH/pDNA with different N/P ratios. (C) The comparison of particle sizes with different N/P ratios. (D) The comparison of zeta

potentials with different N/P ratios. (E) The PDI of DOX/VCPH/pDNA with different N/P ratios. (II) The comparation of zeta potentials in different solvents. (III) The comparation of particle sizes in different solvents. (n = 3).

succinate, the signal peak of H_4 in vitamin E succinate appeared at the chemical shift of 2.98 ppm, and the proton peak at 3.39 ppm was the hydrogen shift (H_6) of –OCH_3 in polyethylene glycol monomethylether. The proton peak in the repeat –OCH_2CH_2 - (H_7) was in the range of 3.4–3.6 ppm, and the –CH_2-COOH (H_8) methyl-was affected by the carboxyl group, with a proton peak at 4.07 ppm. The proton peak of 3.5–3.9 ppm was attributed to the hydrogen (H_a, H_c, H_d, H_e and H_f) signal peaks on the monosaccharide unit of chitosan. The H_{11} signal peak of histidine appeared at the chemical shift of 2.98 ppm, and the H_{12} signal peak of histidine appeared at the chemical shift of 3.76 ppm. The H_{10} signal peak of histidine appeared at 4.43 ppm and the proton peak at 8.08 ppm belonged to the signal peak of H_9 of histidine. The results indicated that vitamin E succinate, polyethylene glycol monomethylether and histidine were successfully grafted onto the amino group of chitosan.

3.3. *Effects of different N/P ratios and solvents on the construction of nanoparticles*

The results of particle sizes, zeta potentials and SEM morphology with different N/P ratios were shown in Fig. 3 (I). It could be seen from the results that the particle size gradually decreased as the N/P ratio increased, indicating that the increase loading of pDNA could enhance its electrostatic interaction with DOX/VCPH, which enhanced the binding force of the nanostructure and prompted their tight combination. DOX/VCPH/pDNA with N/P ratio of 55 had the lowest zeta potential, however, the change of average zeta potential was not obvious between different N/P ratios, with relatively stable surface charge. The results demonstrated that the pDNA and DOX/VCPH nanoparticles were not simply surface-coated, but had a complicated three-dimensional entanglement effect. The SEM results showed that DOX/VCPH/pDNA

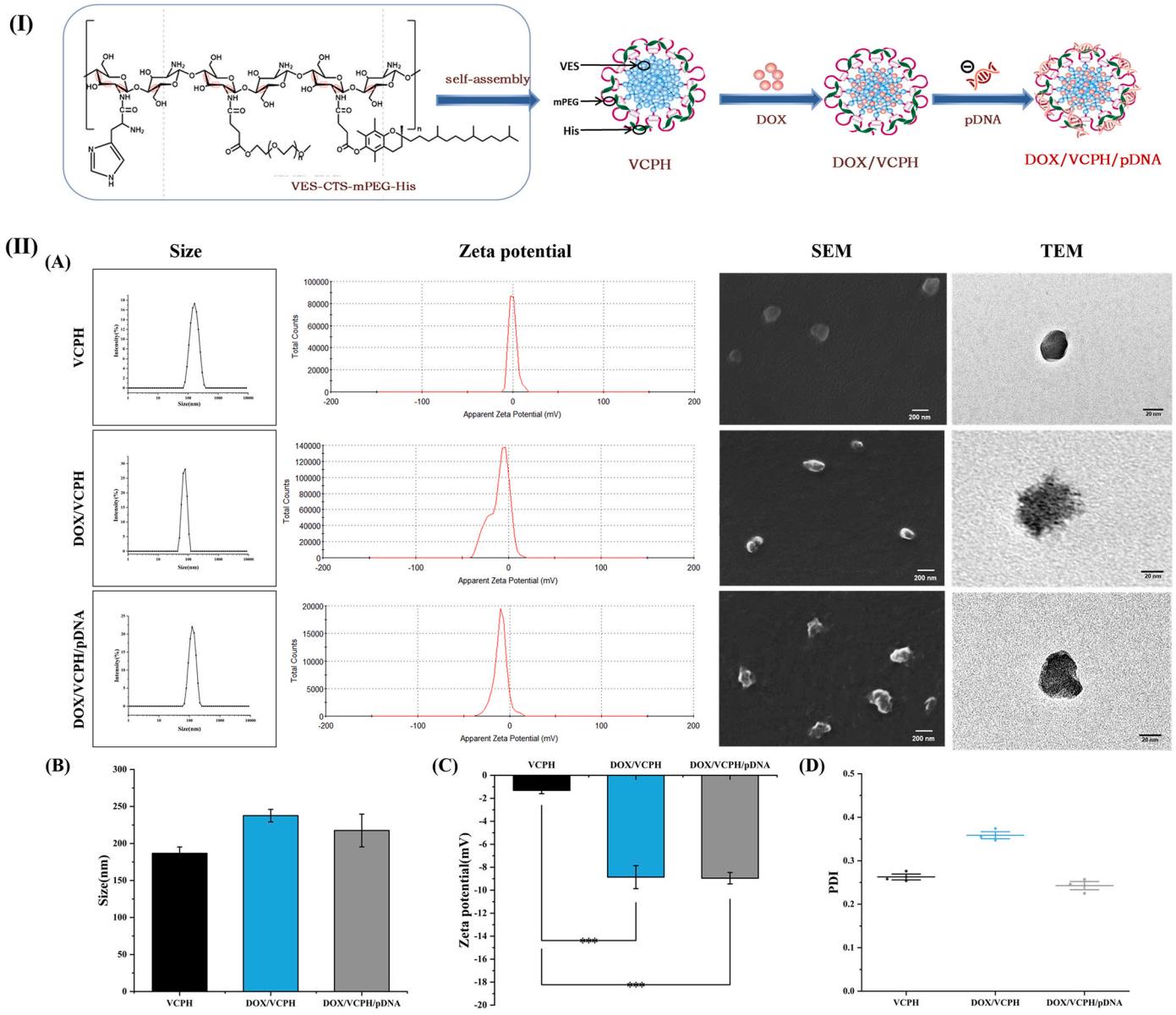

Fig. 4. (I) The self-assembly scheme of VCPH. (II) The particle sizes, zeta potentials, SEM and TEM images of VCPH, DOX/VCPH and DOX/VCPH/pDNA. (Bar = 200 nm in SEM and Bar = 20 nm in TEM, n = 3).

with different N/P ratios all present regular spherical shapes with particle sizes around 200 nm, which were consistent with the DLS results. Based on the above results and transfection efficiency of the different NPs, DOX/VCPH/pDNA with N/P ratio of 55 was finally determined for subsequent experiments.

The zeta potential was closely related to the solvent of the nanoparticles. The results of Fig. 3 (II) showed that the average zeta potential of VCPH nanoparticle was −1.315 ± 0.487 mV in PBS buffer (pH = 7.4). When VCPH combined with DOX, the zeta potential of DOX/VCPH nanoparticles decreased to −8.860 ± 1.738 mV. When DOX/VCPH combined with pDNA, the average zeta potential of DOX/VCPH/pDNA nanoparticles was −8.953 ± 0.863 mV. It could be seen that the combination of DOX and pDNA reduced the surface zeta potentials of the nanoparticles in pH 7.4 buffer. However, this reduction was not obvious in PBS buffer. When the solvent changed to 0.5 % acetic acid, the zeta potential on the surface of the VCPH nanoparticle increased to 32.8 ± 7.3 mV. When VCPH combined with DOX and pDNA, the zeta potentials of DOX/VCPH and DOX/VCPH/pDNA nanoparticles decreased to 28.1 ± 1.3 mV and 15.1 ± 0.21 mV, respectively. Although the combination of DOX and pDNA reduced the value of zeta potential obviously, the DOX/VCPH/pDNA nanoparticles still showed positive zeta potential finally in the solvent of 0.5 % acetic acid. The presence of hydrogen ions in acetic acid solution could affect the surface charge of the nanoparticles, resulting in positive charge on the surface. According to the results above, the average zeta potential could be controlled by selecting suitable solvent.

The effect of different solvents on particle sizes of nanoparticles was shown in Fig. 3 (III). The results showed that the particle size of VCPH was 186.633 ± 15.054 nm and the particle size of DOX/VCPH was 237.600 ± 14.591 in PBS buffer (pH = 7.4). After loading the drug DOX, the particle size increased by about 51 nm. VCPH could carried DOX through self-assembly effect, and DOX was encapsulated in its hydrophobic core. The average particle size of DOX/VCPH increased due to the encapsulation of DOX. When the DOX/VCPH combined with pDNA, the particle size decreased to 217.533 ± 38.322 nm. The pDNA could enhanced the binding force of the nanostructure and prompted their tight combination. When the solvent changed to 0.5 % acetic acid, the particle size of VCPH was 147.6 ± 40.4 nm and the average particle size of DOX/VCPH was 283.2 ± 31.7 nm. After combined with pDNA, the particle size decreased to 267.9 ± 8.9 nm. Chitosan was fully protonated and had high DOX and pDNA loading and binding efficiency in 0.5 % acetic acid solvent, which was speculated to be the reason of the large particle size. According to the results above, the particle size could be changed by selecting suitable solvent.

3.4. Particle sizes, zeta potentials, SEM, TEM and PDI analysis of VCPH, DOX/VCPH and DOX/VCPH/pDNA nanoparticles

It was shown in Fig. 4 (I), driven by hydrophobic forces, VES-CTs-mPEG-His formed nanostructure through self-assembly behavior. The particle size distribution results were shown in Fig. 4 (IIA and IIB). It could be seen that the average particle size of the VCPH was 186.633 ± 15.054 nm, and PDI was 0.317 ± 0.052. VCPH nanoparticles were spherical or ellipsoidal in shape, with a particle size of 100–200 nm. The nanoparticles had uniform distribution and no obvious agglomeration phenomenon, which was consistent with the detection results of DLS. When VCPH carried DOX, the average particle size of drug-loaded nanoparticle DOX/VCPH was 237.600 ± 14.591 nm, and PDI was 0.310 ± 0.042. Compared with the VCPH nanoparticles, the average particle size increased 51 nm, which was due to the encapsulation of DOX. The SEM results showed that the particle size of drug-loaded nanoparticles was between 200 nm and 300 nm, slightly larger than that of VCPH nanoparticles. The shape was spherical, and it had obvious fullness compared with the shape of VCPH nanoparticles. There was no obvious agglomeration of DOX/VCPH nanoparticles, which was consistent with the results of DLS. The average particle size of DOX/VCPH/pDNA was 217.533 ± 38.322 nm, and the PDI was 0.243 ± 0.016. It was observed in the SEM results that DOX/VCPH/pDNA nanoparticles were spherical or ellipsoidal in shape, with a particle size of 200–300 nm. DOX/VCPH/pDNA nanoparticles had uniform distribution, and no obvious agglomeration phenomenon. The average particle size of DOX/VCPH/pDNA was smaller than that of DOX/VCPH, indicating that the loading of pDNA could enhanced the binding force of the nanostructure and prompted their tight combination. The TEM micrographs of VCPH, DOX/VCPH and DOX/VCPH/pDNA was shown in Fig. 4 (IIA). The results showed that the particle sizes were about 100 nm and exhibited a regular structure that was approximately spherical, consistent with the results of SEM.

The zeta potential results were shown in Fig. 4 (IIA and IIC). The zeta potential on the surface of the VCPH nanoparticle was −1.315 ± 0.487 mV. When VCPH combined with DOX and pDNA, the zeta potentials of DOX/VCPH and DOX/VCPH/pDNA nanoparticles decreased to −8.860 ± 1.738 mV and −8.953 ± 0.863 mV, respectively. It could be seen that the combination of DOX and pDNA reduced the surface zeta potentials of the nanoparticles. The low positive charge was beneficial to improve the stability and safety of nanoparticles in blood vessels. However, under the condition of pH 7.4, the charge characteristics of the nanoparticle surface were not ideal for its binding to pDNA. Therefore, in the follow-up study, we studied the influence of solvent on zeta potential and particle size, and improved its loading efficiency through solvent selection.

3.5. Stability result of VCPH nanoparticles under physiological conditions

The stability of VCPH under physiological conditions was crucial for its drug loading capacity and application. The stability could be studied by measuring the particle sizes, zeta potentials, and PDI of VCPH at different times. Results in Fig. 5 showed that the particle sizes, zeta potentials, and PDI of VCPH did not have significant changes over the course of 0, 1, 3, 5, and 7 days. Specifically, the particle sizes remained stable at around 180 nm, the zeta potentials were around −1.6 mV, and the PDI was maintained at around 0.3. These results indicated that VCPH exhibited good stability and dispersibility under physiological conditions.

Fig. 6 (IA) showed the influence of drug carrier mass ratio on encapsulation efficiency and drug loading capacity. The results showed that with the increase of the mass ratio of the drug, the DOX loading capacity increased, but the encapsulation efficiency decreased. Therefore, the ratio DOX and VCPH at 3:5 was selected to prepare drug-loaded nanoparticles for subsequent research, to ensure high drug loading and avoid drug waste caused by too low encapsulation efficiency. The drug loading capacity was calculated to be 31.58 ± 2.91 %, and the encapsulation efficiency was 84.21 ± 7.77 %.

3.6. Encapsulation efficiency and drug loading capacity of DOX/VCPH

The π-π conjugation of DOX/VCPH was determined by ultraviolet spectrophotometer. The conjugation between DOX and VCPH molecules had an important relationship with the delocalization energy of electrons, which could make the whole conjugated system more stable. After the conjugation happened, the mobility of π electrons increased while the transition energy decreased. The absorption peak occurred redshift phenomenon, and the spectral wavelength became longer. Fig. 6 (IB) showed that DOX·HCl had its maximum absorption peak at 485 nm, while DOX/VCPH had its maximum absorption peak at 496 nm. DOX/VCPH had a redshift compared to DOX·HCl, indicating that π-π conjugation forces occurred during the process of VCPH encapsulating DOX. And the π-π conjugation made the DOX/VCPH system more stable.

3.7. Drug release behavior of DOX/VCPH in vitro

The drug release behavior of DOX/VCPH in normal tissues (pH =

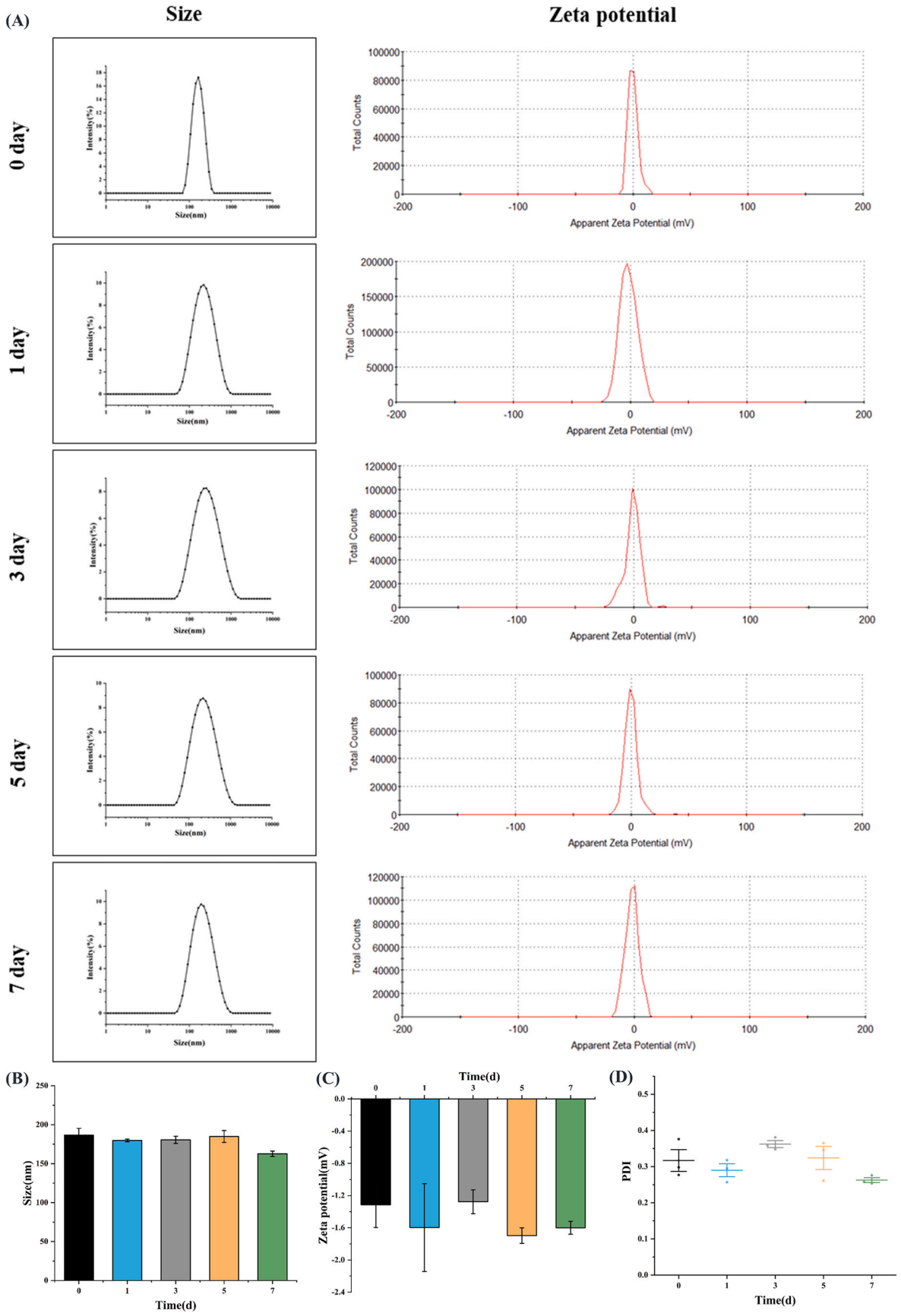

Fig. 5. (A) The particle sizes and zeta potentials of VCPH at different days. (B) The comparison of particle sizes at different days. (C) The comparison of zeta potentials at different days. (D) The PDI of VCPH at different days. (n = 3).

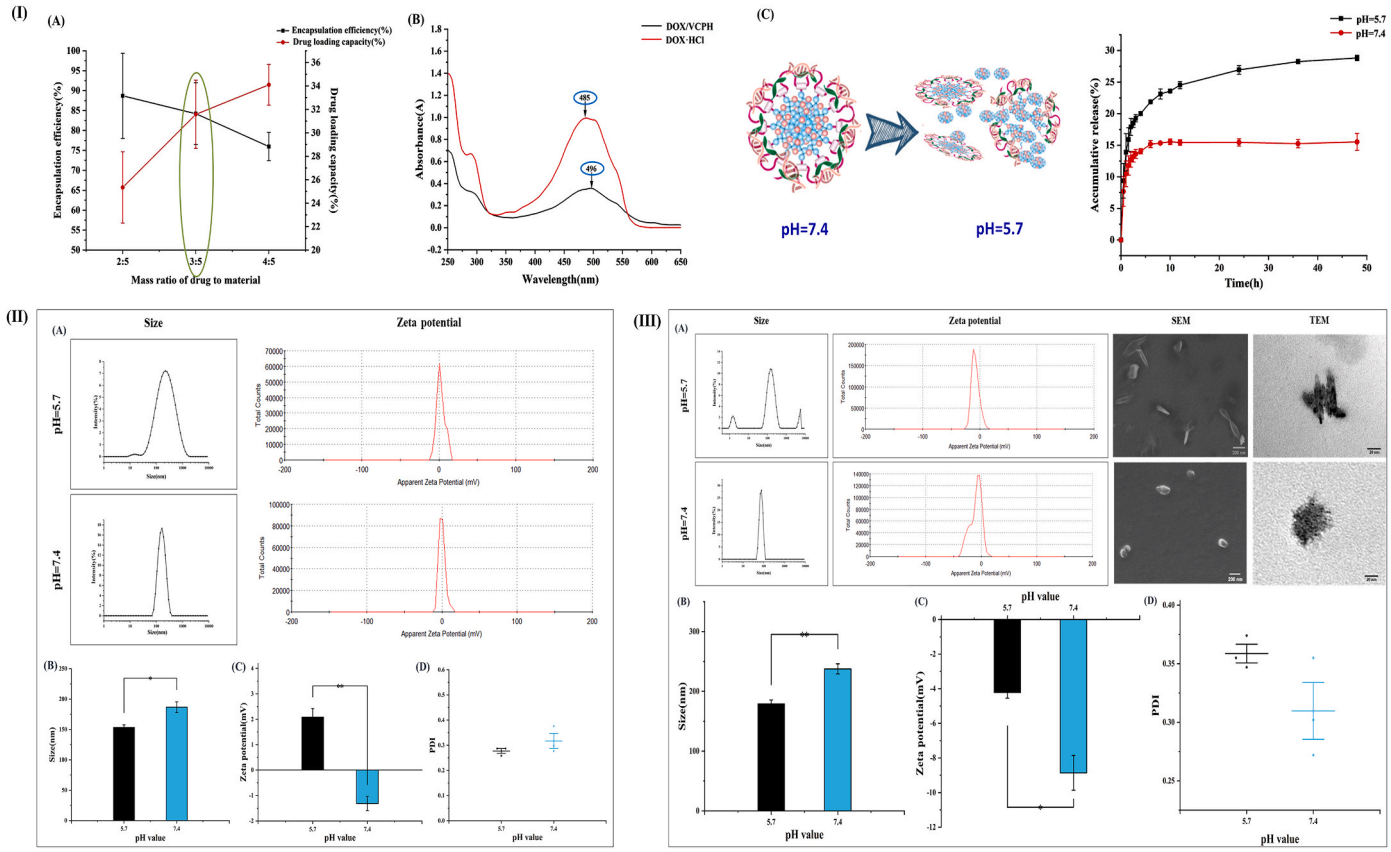

Fig. 6. (I) Drug loading and release behavior of VCPH. (A) The LC and EE with different mass ratios of DOX and VCPH. (B) UV–vis spectra of amphiphiles of DOX/VCPH and DOX·HCl. (C) *In vitro* release of DOX/VCPH nanoparticles in PBS buffer solution with different pH values. (II) pH sensitivity of VCPH. (A) The particle sizes and zeta potentials of VCPH with different pH values. (B) The comparison of particle sizes with different pH values. (C) The comparison of zeta potentials with different pH values. (D) The PDI of VCPH with different pH values. (III) pH sensitivity of DOX/VCPH. (A) The particle sizes, zeta potentials and morphology of DOX/VCPH with different pH values. (B) The comparison of particle sizes with different pH values. (C) The comparison of zeta potentials with different pH values. (D) The PDI of DOX/VCPH with different pH values. (*$P < 0.05$, **$P < 0.01$, n = 3).

7.4) and tumor tissues (pH = 5.7) was simulated by dialysis. As shown in Fig. 6 (IC), both in PBS buffers with pH = 5.7 and pH = 7.4, drugs had different release rates at different stages. In the first 0.5 h, DOX/VCPH showed a fast release behavior, and in the subsequent 0.5–48 h, DOX/VCPH showed very low release rate. However, at the end, the cumulative release of the drug was different in the two different pH environments. At 48 h, the cumulative doxorubicin release of DOX/VCPH nanoparticles was 28.72 % in PBS buffer with pH of 5.7, but only 15.53 % doxorubicin was released in PBS buffer with pH of 7.4. Therefore, the drug release behavior of DOX/VCPH nanoparticles was typically pH responsive, and it released quickly under acidic conditions.

3.8. pH sensitivity of VCPH nanoparticles

The pH sensitivity of VCPH could be studied by measuring the changes in particle sizes, zeta potentials, and PDI under different pH conditions. The results in Fig. 6 (II) showed that when the pH was 7.4, the particle size of VCPH was 186.633 ± 15.054 nm, the average zeta potential was −1.315 ± 0.487 mV, and the PDI was 0.317 ± 0.052. At pH 5.7, the particle size of VCPH was 153.533 ± 7.100 nm, the average potential was 2.083 mV, and the PDI was 0.277. The difference in particle size between the two conditions was about 30 nm, which was due to the loose dissociation of VCPH nanostructures and some of them break into fragments, resulting in a smaller particle size. The slight increase in zeta potential at pH 5.7 was due to the binding of H^+ in the solvent. The PDI values were not significantly different and both were less than 0.5, indicating good dispersibility of VCPH. The results showed that the change in particle size of VCPH was conducive to the release of DOX in the tumor environment.

3.9. pH sensitivity of DOX/VCPH nanoparticles

The pH sensitivity of DOX/VCPH was studied by measuring the changes in particle size, zeta potential, and morphology at different pH values. The results in Fig. 6 (III) showed that the average particle size of DOX/VCPH decreased from 237.600 ± 14.591 nm to 179.167 ± 11.361 nm when the pH value was reduced from 7.4 to 5.7. SEM and TEM results revealed that the structure of DOX/VCPH dissociated and broke down from regular ellipsoid shapes into irregular rod-like, needle-like structures, and fragments. Therefore, the decrease in particle size was related to the structural damage and partial drug release in pH 5.7 condition. These fragments and their aggregates caused the appearance of interference peaks in the DLS results.

The average potential changed from −8.860 ± 1.738 mV to −4.217 ± 0.562 mV, showing a slight decrease, which was related to the combination of H^+ in acidic environment and the release of DOX. There was no significant change in PDI, which was from 0.310 ± 0.042 to 0.359 ± 0.014. The above results indicated that when DOX/VCPH in acidic environment, its near-spherical particle structure would undergo significant disassembly, which would accelerate the release of DOX and endow the nano-carrier with sensitive responsiveness to acidic microenvironment.

3.10. Cytotoxicity and hemolytic tests results of different nanoparticles

Fig. 7 (A) showed the relative proliferation rate of L929 cells treated

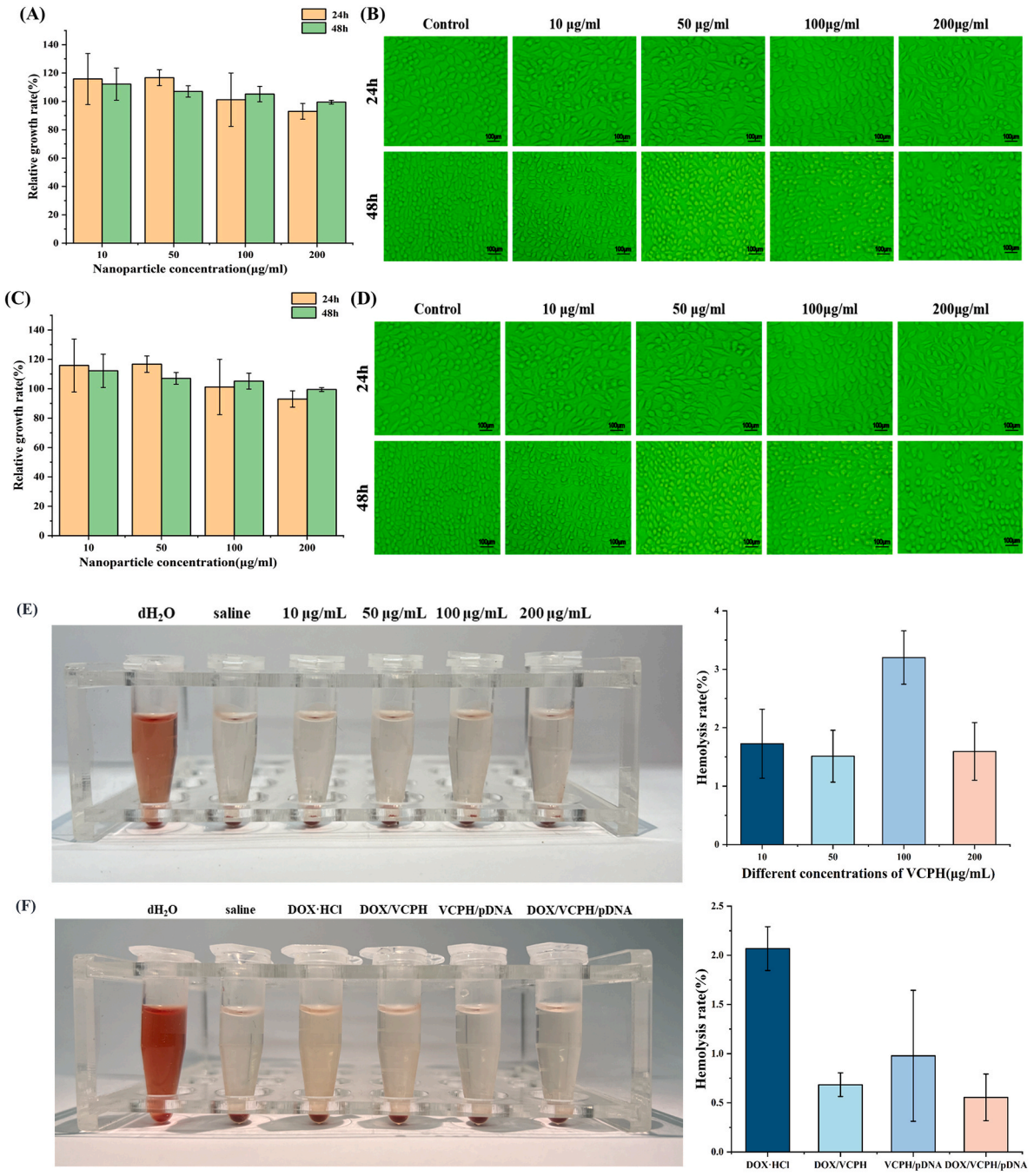

Fig. 7. (A) Cytotoxicity of VCPH on L929 cells. (n = 6) (B) The growth condition of L929 cells incubated with different concentration of VCPH. (C) Cytotoxicity of VCPH on A549 cells. (n = 6) (D) The growth condition of A549 cells incubated with different concentration of VCPH. (E) Hemolytic evaluation of VCPH. (n = 5) (F) Hemolytic evaluation of different nanoparticles. (n = 5).

with different concentrations of VCPH nanoparticles by MTT assay after 24 h and 48 h growth. All the relative cell proliferation rates of each group were above 80 %. According to the cytotoxicity rating, the cytotoxicity rates were level 0 or level 1 with no cytotoxicity, indicating that the VCPH nanoparticles had good cytocompatibility. Fig. 7 (B) showed the morphology of L929 cells cultured in fresh medium with different concentrations of VCPH nanoparticles for 24 h and 48 h. After 24 h and 48 h growth in the medium with different concentrations of nanoparticles, L929 cells grew and proliferated normally, showing normal spindle-shaped or flat cell morphology. The number of cells observed under the microscope was roughly the same as that in the control group, with no significant difference. No obvious apoptotic phenomena such as cell deformation, contraction or cell separation was found.

Fig. 7 (C) showed the relative proliferation rate of A549 cells treated with different concentrations of VCPH nanoparticles by MTT assay after 24 h and 48 h growth. All the relative cell proliferation rates of each group were above 80 %. According to the cytotoxicity rating, the cytotoxicity rates were level 0 or level 1 with no cytotoxicity, indicating that the VCPH nanoparticles had good cytocompatibility. Fig. 7 (D) showed the morphology of A549 cells cultured in fresh medium with different concentrations of VCPH nanoparticles for 24 h and 48 h. After 24 h and 48 h growth in the medium with different concentrations of nanoparticles, A549 cells grew and proliferated normally, showing normal spindle-shaped or flat cell morphology. The number of cells observed under the microscope was roughly the same as that in the control group, with no significant difference. No obvious apoptotic phenomena such as

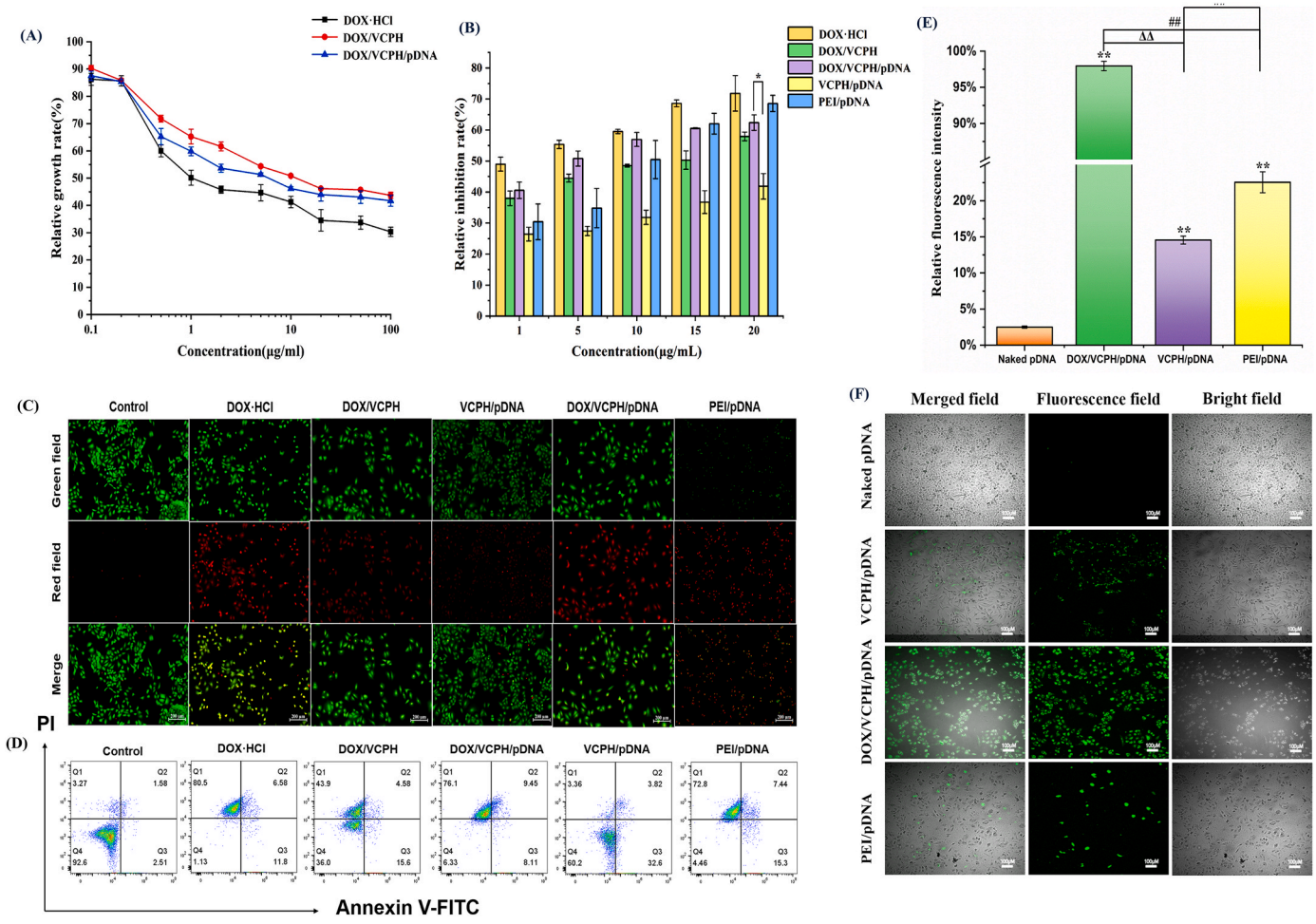

Fig. 8. (A) IC_{50} results of DOX·HCl、DOX/VCPH、DOX/VCPH/pDNA nanoparticles with different DOX concentrations against A549 cells. (n = 6) (B) The relative inhibition rate of A549 cells transfected with different nanoparticles ($^{*}P < 0.05$, n = 6). (C) The Calcein/PI staining images of A549 cells with different nanoparticles. (n = 3) (D) The flow cytometry result of A549 cells with different nanoparticles. (n = 3) (E) GFP-positive rate detected by flow cytometry of A549 cells transfected with different nanocomposite particles(compared with the negative control group, $^{**}P < 0.01$, compared with the positive control group, $^{\#\#}P < 0.01$, compared between DOX/VCPH/pDNA and VCPH/pDNA, $^{\triangle\triangle}P < 0.01$, n = 6). (F) Laser confocal scanning microscopy of A549 cells transfected with different nanocomposite particles. (n = 3).

cell deformation, contraction or cell separation was found.

The result of hemolytic evaluation was shown in Fig. 7 (E and F). The hemolysis rate above 5 % was generally considered to be hemolysis. The results showed that all the samples had good blood compatibility, and the hemolysis rates were much lower than 5 %.

3.11. IC_{50} determination and antitumor effect of DOX/VCPH/pDNA in vitro

Fig. 8 (A) showed the IC_{50} test results of DOX·HCl, DOX/VCPH and DOX/VCPH/pDNA on A549 cells. It could be seen from the figure that the IC_{50} of DOX·HCl, DOX/VCPH, DOX/VCPH/pDNA on A549 cells at 24 h was 1.39 μg/mL, 12.50 μg/mL and 6.95 μg/mL, respectively. As shown in Fig. 8 (B), with the increase of DOX concentration, the inhibitory effects of DOX·HCl, DOX/VCPH, DOX/VCPH/pDNA, PEI/pDNA, and VCPH/pDNA on the growth of A549 cells were significantly increased. When DOX concentration was 20 μg/mL, the growth of A549 cells could be significantly improved. The cell growth inhibition rate of DOX·HCl was 71.81 %, the cell growth inhibition rate of DOX/VCPH was 57.93 %, the cell growth inhibition rate of VCPH/pDNA was 41.85 %, and the cell growth inhibition rate of PEI/pDNA was 68.56 %. Compared with DOX/VCPH and VCPH/pDNA, the cell growth inhibition rate of dual-loaded nanoparticles DOX/VCPH/pDNA was higher, which reached 62.40 %. DOX/VCPH/pDNA showed significant differences compared with VCPH/pDNA, indicating that dual-loaded nanoparticles DOX/VCPH/pDNA had better anti-tumor effects than DOX/VCPH and VCPH/pDNA *in vitro*.

3.12. Calcein/PI staining result of A549 cells with different nanoparticles

The lipophilicity of methyl acetate of Calcein-AM was very high, which could penetrate through the cell membrane. The AM group was removed by the action of esterase in living cells, and the generated Calcein emitted strong green fluorescence (excitation: 490 nm, emission: 515 nm). Therefore, living cells could be detected under a fluorescence microscope to emit green fluorescence. PI, as a nuclear staining dye, couldn't pass through the cell membrane of living cells. It passed through the disordered area of dead cell membrane to reach the nucleus and embeded into the DNA double helix of cells to generate red fluorescence (excitation: 530 nm, emission: 620 nm). Therefore, PI could stain dead cells. The combined use of Calcein-AM and PI could simultaneously perform double fluorescent staining of living cells and dead cells. Calcein and PI could both be excited by 490 nm, so living cells and dead cells could be observed simultaneously under a fluorescence microscope. While excited by 545 nm, only dead cells could be observed.

Fig. 8 (C) showed the Calcein/PI staining results of A549 cells

cultured in media containing different nanoparticles for 24 h. The results indicated that the control group exhibited the strongest green fluorescence intensity and the largest number of green cells in all groups, followed by the VCPH/pDNA group. The DOX·HCl group and the DOX/VCPH/pDNA group displayed less green fluorescence. The results for red fluorescence signals were opposite to those for green fluorescence, with the DOX·HCl group and the DOX/VCPH/pDNA group showing strong red fluorescence, while the control group displayed very few red fluorescence signals. These results suggested that compared to the control group, the nanoparticles in all group had effect on the apoptosis of A549 cells, with the DOX·HCl group and the DOX/VCPH/pDNA group showing the strongest apoptosis-promoting effects. Due to the cytotoxicity of PEI, the majority of cells cultured with PEI/pDNA for 24 h underwent apoptosis, with disrupted cell morphology and mostly consisting of cell debris, resulting in weak fluorescence intensity.

3.13. Flow cytometry result of A549 cells with different nanoparticles

Fig. 8 (D) showed the flow cytometry analysis, which was consistent with the Calcein/PI staining results. The percentage of live cells in the control group was 92.6 %, while the percentages of live cells in the DOX/VCPH group and VCPH/pDNA group were 36.0 % and 60.2 %, respectively. The percentage of live cells in the DOX/VCPH/pDNA group was only 6.33 %, which was close to the results of the positive control groups (DOX·HCl and PEI/pDNA groups) with the percentage of 1.13 % and 4.46 %, respectively. The results indicated the significant inhibitory effect of DOX/VCPH/pDNA on A549 cells.

3.14. Transfection efficiency of DOX/VCPH/pDNA in A549 cells

The delivery and expression of A549 cells transfected with different nanoparticles for 48 h were shown in Fig. 8 (E and F). The naked pDNA group was used as the negative control group and the PEI/pDNA group was used as the positive control group. The positive rate of transfection of A549 cells with different nanoparticles was detected by flow cytometry. The results in Fig. 8 (E) showed that the transfection rate of DOX/VCPH/pDNA group was the highest, reaching 98.3 %. While that of VCPH/pDNA group was 15.1 % and that of PEI/pDNA group was 21 %. Furthermore, DOX/VCPH/pDNA group had extremely significant differences compared with the naked pDNA group, the PEI/pDNA group and VCPH/pDNA group. The result of CLSM of A549 cells transfected with different nanoparticles for 48 h was shown in Fig. 8 (F). The naked

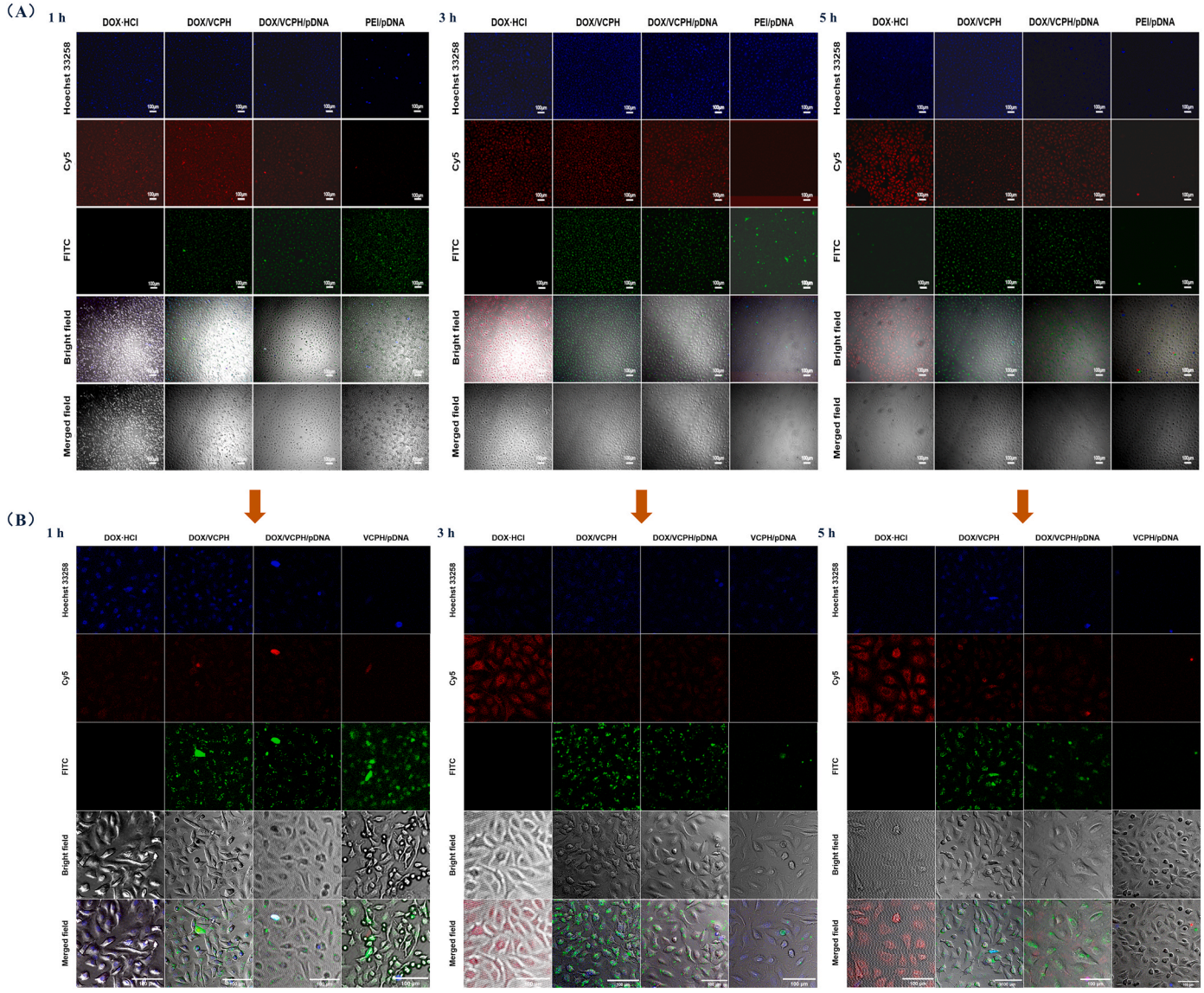

Fig. 9. (A) Confocal laser observation of A549 cells transfected with different labeled nanocomposite particles for 1h, 3h and 5 h (Bar = 100 μm) (B) The magnified pictures of Fig. 5 (A). (Bar = 100 μm, n = 3).

pDNA group showed no fluorescence signal, while the fluorescence signals were observed in several groups containing different nanoparticles. VCPH/pDNA group, DOX/VCPH/pDNA group and PEI/pDNA group all showed strong fluorescence expression intensity and quantity, among which the expression quantity and intensity of VCPH/pDNA group were weaker than that of positive control PEI/pDNA group, while the green fluorescence expression quantity and intensity of DOX/VCPH/pDNA group were the highest.

3.15. DOX/VCPH/pDNA tracing in A549 cells

The process and distribution of DOX/VCPH/pDNA nanoparticles transfected into A549 cells were shown in Fig. 9. The nucleus was blue after stained by Hoechst 33258 dye. VCPH was green after labeled by FITC. The Cy5-labeled pDNA and DOX were red. After 1 h of transfection, the intensity of blue fluorescence, red fluorescence and green fluorescence in all groups was not obvious, and the composite particles had entered the cells. After transfection for 3 h, DOX·HCl group showed strong red fluorescence in the nucleus, while DOX/VCPH group showed stronger red fluorescence in the cytoplasm, and both DOX/VCPH/pDNA group and VCPH/pDNA group showed red fluorescence in the cytoplasm and nucleus. These results indicated that DOX·HCl entered the nucleus quickly due to free diffusion effect. However, due to endosome-lysosome endocytosis, nanoparticles entered cells slowly. After transfection for 5 h, the blue fluorescence, red fluorescence and green fluorescence of each group basically overlapped, indicating that DOX and pDNA carried by VCPH had been delivered to the nucleus.

3.16. Results of relative changes in body weights in nude mice

The antitumor activity study *in vivo* was carried out as shown in Fig. 10 (A). The first day of initiation of administration was marked as day 0, and the relative changes in body weight of nude mice during treatment were shown in Fig. 10 (B). The figure showed that the body weights of nude mice in the control group had been increasing, and the body weights of DOX·HCl group had a significant decreasing trend since the second dose, and the body weights showed an increasing change on the 12th day after administration. There was also weight loss in DOX/

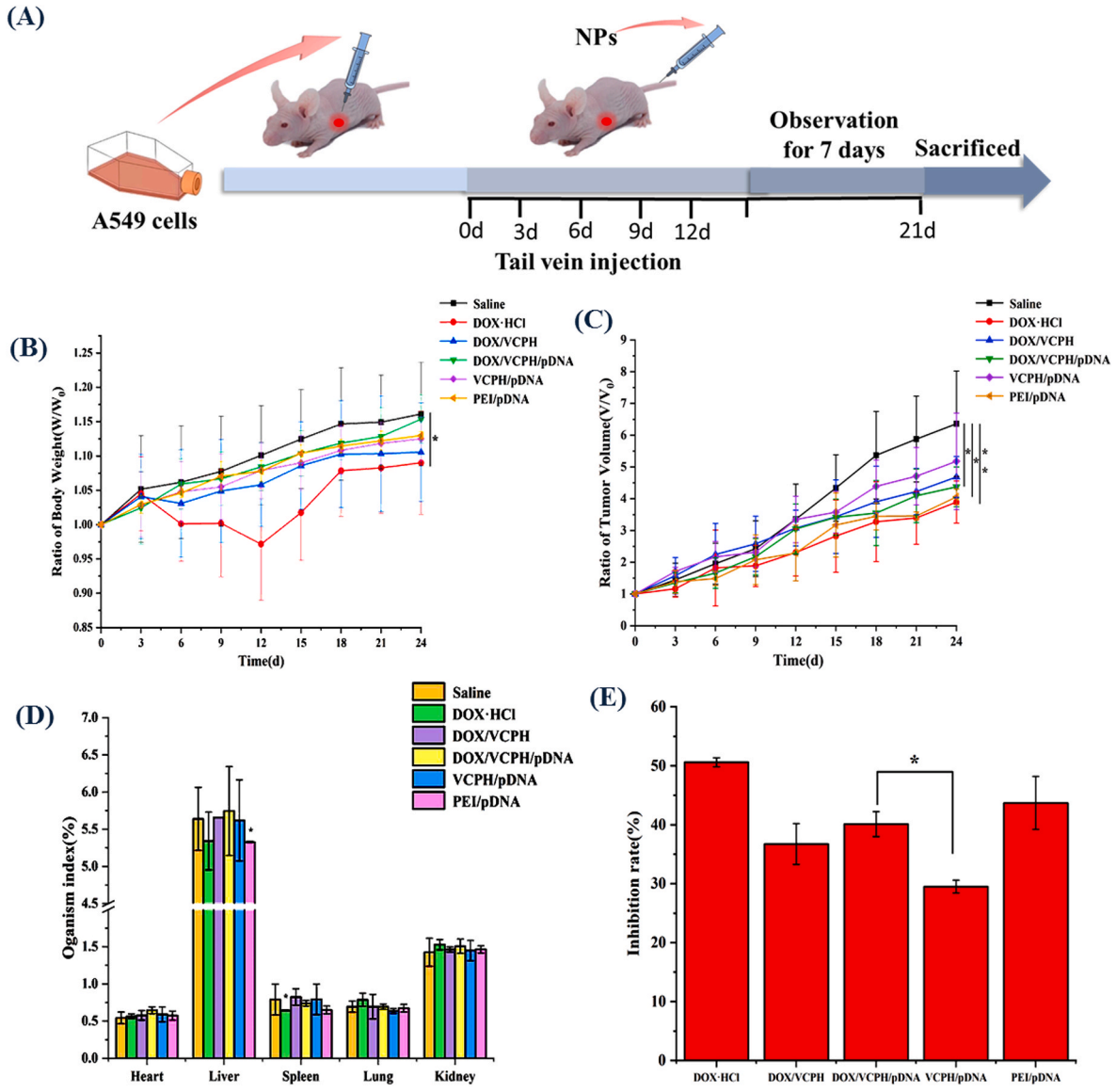

Fig. 10. (A) Schematic diagram of anti-tumor experiment *in vivo*. (B) The relative weight changes of nude mice in different nanoparticle groups (compared with saline group, $^{*}P < 0.05$) (C) The relative changes of tumor diameter in nude mice with different nanoparticle groups (compared with saline group, $^{*}P < 0.05$, $^{**}P < 0.01$) (D) Viscera index of major organs of nude mice in different groups (compared with saline group, $^{*}P < 0.05$). (E) *In vivo* tumor inhibition rate of different groups of nude mice (compared between DOX/VCPH/pDNA and VCPH/pDNA, $^{*}P < 0.05$) (n = 6).

VCPH group after administration, but the degree of decrease was relatively low, and then gradually increased. The body weight of DOX/VCPH/pDNA group, VCPH/pDNA group and PEI/pDNA group increased, respectively. After 24 days of administration, there was a significant difference between the DOX·HCl group and the physiological salt group, but no significant difference between the other four groups. DOX caused weight loss in nude mice due to its toxic and side effects, while DOX/VCPH/pDNA group did not cause weight loss in nude mice, indicating that VCPH could reduce the toxic effects of DOX.

3.17. Results of relative changes in tumor volume in nude mice

The first day of administration was marked as day 0. Fig. 10 (C) showed the relative changes of tumor volume in nude mice with different nanoparticle groups after 24 days of treatment. The tumor volume of nude mice in the control group kept on a rising period. After 24 days of treatment, the tumor volume in the control group increased to 6.36 times of the initial volume. While the tumor volume in the DOX·HCl group, DOX/VCPH group, DOX/VCPH/pDNA group, VCPH/pDNA group and PEI/pDNA group increased to 3.89, 5.18, 4.37, 4.69 and 4.06 times of the initial volume, respectively. After 24 days of treatment, DOX·HCl group showed significant differences compared with physiological salt group; DOX/VCPH/pDNA group and PEI/pDNA group showed significant differences compared with physiological salt group, while the other two groups showed no significant differences. There was no significant difference in DOX/VCPH/pDNA group compared with positive control DOX·HCl group and PEI/pDNA group. The results of the relative changes of tumor volume in nude mice showed that the tumor volume changes in DOX/VCPH/pDNA group had obvious advantages over those in DOX/VCPH and VCPH/pDNA groups, indicating that DOX/VCPH/pDNA had a better effect of inhibiting tumor growth.

3.18. Organ index of nude mice

After treatment, the organ index of nude mice in each group was calculated as shown in Fig. 10 (D). As could be seen from the figure, there was no significant difference in organ indices of tissues in DOX/VCPH group, VCPH/DNA group and DOX/VCPH/DNA group compared

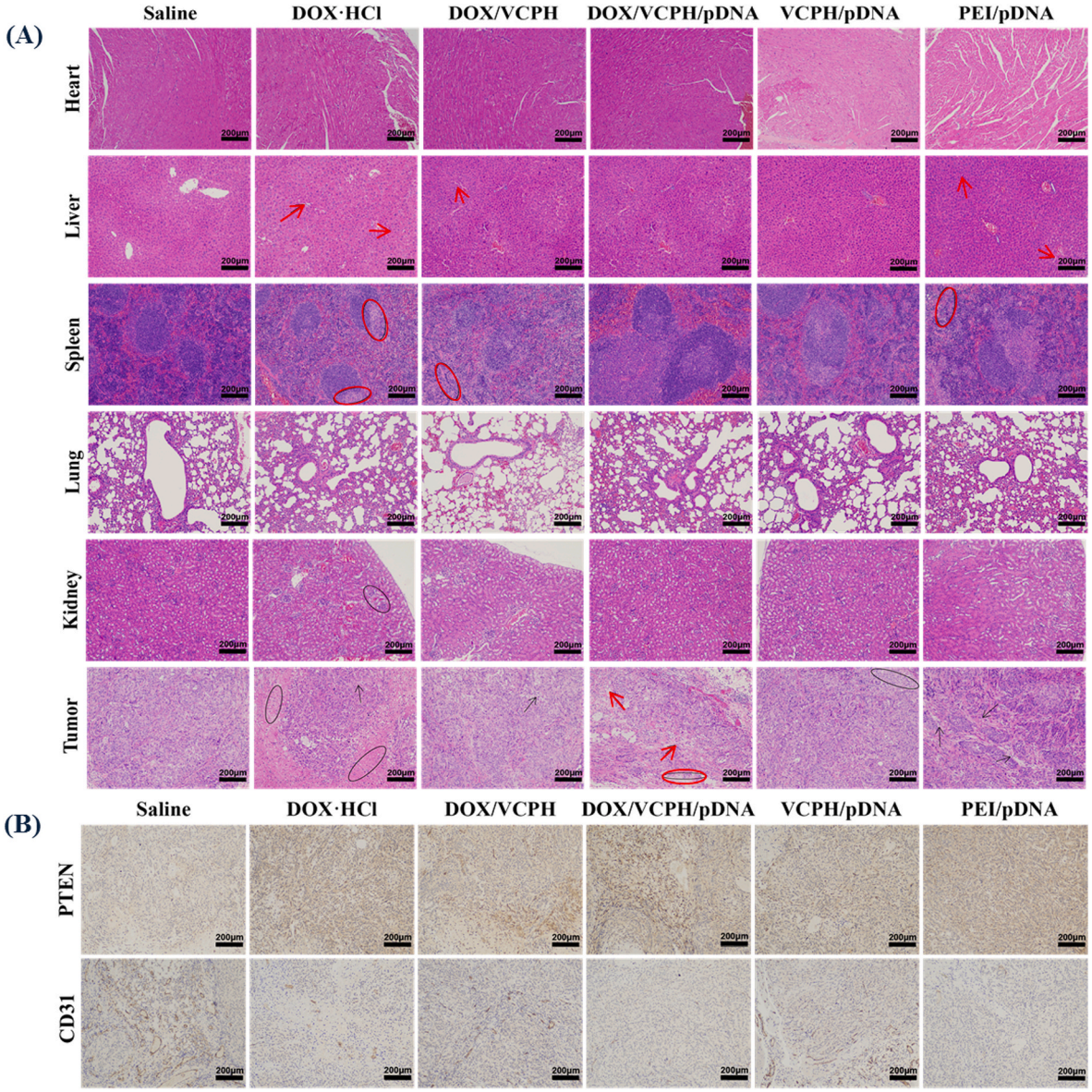

Fig. 11. (A) H&E staining of the main organs of nude mice in different groups. (B) Immunohistochemical images of PTEN and CD31 in tumor sections from different groups of nude mice. (n = 3).

with saline group. While the spleen of DOX·HCl group and the liver of PEI/pDNA group showed significant differences compared with saline group, indicating that DOX and PEI had certain toxic effects on normal organ tissues of nude mice and the VCPH could decrease the toxicity.

3.19. Tumor inhibition effect in nude mice

After the treatment, the nude mice were killed, and the tumor bodies of each group were stripped and photographed. The pictures of tumors were shown in Fig. 10 (E). The results were consistent with the trend of relative tumor volume change in nude mice during treatment. Calculated to the tumor inhibition rate formula, the tumor inhibition rates were 50.60 %, 43.71 %, 36.72 %, 29.49 % and 40.12 % in DOX·HCl group, PEI/pDNA group, DOX/VCPH group, VCPH/pDNA group and DOX/VCPH/pDNA group, respectively. The DOX/VCPH/pDNA showed better anti-tumor effects *in vivo* compared with DOX/VCPH and VCPH/pDNA, which demonstrated good synergistic effect.

3.20. H&E observation of tissue slices of nude mice

The heart, liver, spleen, lung, kidney and tumor tissues of nude mice in each group were dehydrated, embedded, sliced and stained by H&E, and histopathological observation was made by optical microscope. H&E staining results of nude mice in each group were shown in Fig. 11 (A). The myocardial cells in each group were closely arranged in normal shape, and there was no obvious difference of striated muscle between different groups. In the liver tissues of DOX·HCl group and PEI/pDNA group, it was found that there were large cell gaps, loose cell arrangement, partial deformation and cavitation, and a small amount of loose and irregular liver cells in DOX/VCPH group. Spleen cells in DOX·HCl group and PEI/pDNA group showed morphological changes and loose cells, with certain inflammation and necrosis, while some spleen cells in DOX/VCPH group showed loose and a little tightly arranged cells. Some lung cells in DOX·HCl group showed dilatation and damage, while the lung cells in other groups were closely arranged with clear bronchus and normal shape. Some renal cells in DOX·HCl group showed swelling and inflammation, while some renal cells in PEI/pDNA group showed irregular morphology and loose cells. Both DOX and PEI caused damage to body organs of nude mice due to their respective toxic and side effects, while the body organs of DOX/VCPH/pDNA group were arranged neatly and tightly, with normal morphology, and did not cause loose, dilated, atrophy and inflammation. In the tumor tissues, the cells in the physiological salt group grew vigorously, and it was observed that the stained blue nuclei were closely arranged without necrotic areas, while the tumor tissues in the other groups showed different degrees of damage, and the tumor cells in the DOX/VCPH/pDNA group were loose, disordered and irregularly arranged. The nuclei atrophy, apoptosis and necrosis of the cells occurred, indicating that DOX/VCPH/pDNA group could significantly inhibit the growth of tumor cells and induce apoptosis of tumor cells.

3.21. Immunohistochemical observation of tumor tissues in nude mice

After dehydration, embedding and section treatment, the tumor tissues of nude mice in each group were stained with PTEN and CD31, respectively. And the immunohistochemical observation was performed on the tumor tissues of nude mice. The results were shown in Fig. 11 (B). Hematoxylin stained nucleus was blue, and the positive expression of DAB was brownish-yellow.

Phosphatase and tensin homolog (PTEN) was a protein encoded by PTEN gene in human body. PTEN acted as a tumor suppressor gene through its phosphatase protein product. PTEN was the first tumor suppressor gene with double characteristic phosphatase activity, which had double specificity of lipid phosphatase and protein phosphatase. PTEN played an important role in the regulation of multiple intracellular signaling pathways. The activity of PTEN lipid phosphatase could dephosphorylate phosphatidylinositol triphosphate (PIP3) into phosphatidylinositol diphosphate and inactivate it, and then inhibited the Pl3K/AKT pathway, inhibiting the growth of tumor cells and regulate the cell cycle. The PTEN positive substance in the immunohistochemical results of PTEN was brown-yellow granular, located in the cytoplasm, and visible in the cell membrane or nuclear membrane. As could be seen from Fig. 11 (B), the physiological salt group was normal tumor tissue, there was no brown-yellow positive substance, and the positive rate of PTEN was very low, while the tumor tissue of DOX·HCl group and PEI/pDNA group contained a large number of brown-yellow particles and a small number of nuclei, indicating that the positive rate of PTEN was higher in DOX·HCl group and PEI/pDNA group. Compared with DOX/VCPH and VCPH/pDNA groups, the brown-yellow particles in DOX/VCPH/pDNA group were darker, the number of nuclei was less, and the positive rate of PTEN was significantly higher, indicating that DOX/VCPH/pDNA could significantly inhibit the growth and proliferation of tumor cells.

The platelet-endothelial cell adhesion molecule (CD31) was usually located in vascular endothelial cells, platelets, macrophages and lymphocytes, and its expression was also found in some tumors such as epithelioid hemangioendothelioma. In immunohistochemistry, CD31 was mainly used to prove the existence of endothelial cells and to evaluate tumor angiogenesis. The process of its expression meant the process of rapid tumor growth. The immunohistochemical method of CD31 was of great significance for the diagnosis and treatment of tumors. Fig. 11 (B) showed CD31 positive substances were brown-yellow granules with a high expression rate in the physiological salt group, indicating that normal tumor tissues in the physiological salt group grow rapidly, while the positive rate of tumor tissues in other groups was lower than that in the physiological salt group. Among them, the positive rate of CD31 in DOX/VCPH/pDNA group was significantly lower than that in DOX/VCPH and VCPH/pDNA groups, indicating that VCPH could significantly reduce the formation of tumor blood vessels and inhibit the growth of tumor tissues by the delivery of DOX and pDNA in nude mice.

3.22. The mRNA expression of STAT3 genes in tumor tissues of nude mice

Total RNA was extracted from tumor tissue homogenates of nude mice in each group, and the mRNA expression of STAT3 gene in tumor tissues of nude mice in each group was detected by real-time quantitative PCR. The results were shown in Fig. 12 (A). It could be seen that STAT3 mRNA expression was higher in DOX·HCl group and DOX/VCPH group than other groups. It showed that the gene transcription was not inhibited or interfered with DOX·HCl or DOX/VCPH. The mRNA assays of PEI/pDNA group, VCPH/pDNA group and DOX/VCPH/pDNA group were lower than those of physiological salt group, which were 35.2 %, 59.25 % and 50.12 %, respectively, showing significant differences with physiological salt group, and the mRNA assay of PEI/pDNA group was the lowest. VCPH/pDNA group and DOX/VCPH/pDNA group had extremely significant differences with PEI/pDNA group, while the mRNA assay of DOX/VCPH/pDNA group was lower than that of VCPH/pDNA group, and was significantly different from that of VCPH/pDNA group. These results indicated that VCPH, as a gene carrier, could effectively mediate the transfection of recombinant plasmid pDNA containing STAT3-shRNA into nude mice and successfully delivered the recombinant plasmid, which could inhibit the transcription of STAT3, achieve gene silencing, and inhibit the growth and proliferation of tumors.

3.23. The protein expression of STAT3 in tumor tissue of nude mice

The protein expression level of STAT3 in tumor tissues of nude mice in each group was detected by Western Blot. As shown in Fig. 12 (B), electrophoretic bands in DOX/VCPH/pDNA group, PEI/pDNA group and VCPH/pDNA group were decreased compared with physiological

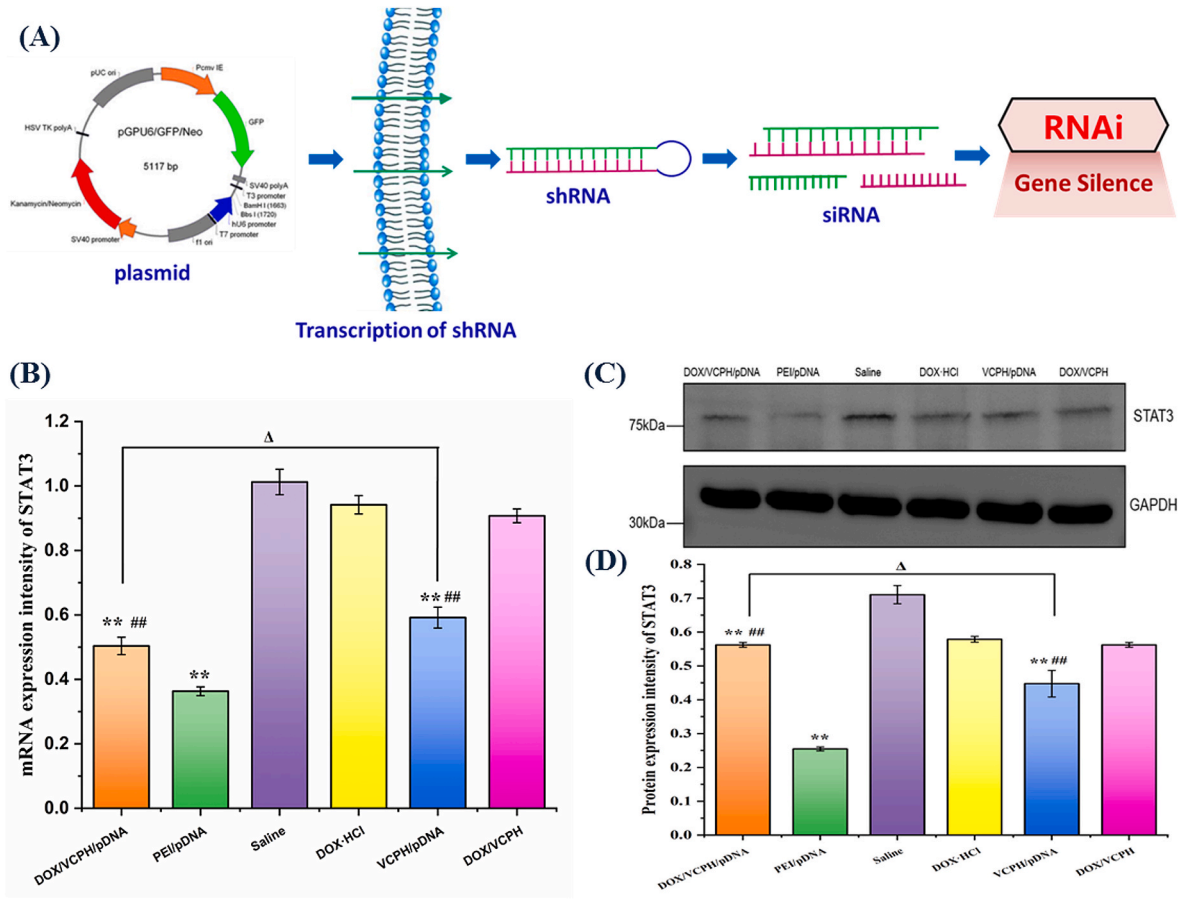

Fig. 12. (A) The transcription and RNAi effect of shRNA. (B) Real-time quantitative PCR was used to detect the mRNA expression of STAT3 in nude mouse tumors (compared with saline group, $^{**}P < 0.01$, compared with the positive control group, $^{\#\#}P < 0.01$, compared between DOX/VCPH/pDNA and VCPH/pDNA, $^{\triangle}P < 0.05$). (C) The electrophoretic map of STAT3 protein expression level in nude mouse tumors was detected by western blot. (D) Western blot was used to detect the protein expression of STAT3 in nude mouse tumors (compared with saline group, $^{**}P < 0.01$, compared with the positive control group, $^{\#\#}P < 0.01$, compared between DOX/VCPH/pDNA and VCPH/pDNA, $^{\triangle}P < 0.05$) (n = 6).

salt group. PEI/pDNA group showed the most obvious dilution, followed by DOX/VCPH/pDNA group. Through the gray scale analysis of protein bands, as shown in Fig. 12 (C), the relative expression levels of proteins in DOX/VCPH/pDNA group, PEI/pDNA group and VCPH/pDNA group were 54.58 %, 35.52 % and 62.43 % ccompared to those in physiological salt group, respectively, showing significant differences compared with physiological salt group. DOX/VCPH/pDNA group and VCPH/pDNA group had extremely significant differences with PEI/pDNA group. DOX/VCPH/pDNA group had lower protein expression level than VCPH/pDNA group, and the two groups had significant differences. GAPDH was used as the reference, and there was no significant difference in the expression levels of all groups. The results indicated that VCPH loaded with STAT3-shRNA recombinant plasmid could interfere with the expression of STAT3 protein in nude mic, reduce the relative expression level of STAT3 protein in nude mice, and thus inhibit the growth and proliferation of tumors.

4. Conclusion

In summary, a self-assembled VCPH nanocarrier has been successfully developed, which can achieve efficient drug and gene combination loading through π-π stacking and charge interaction, and has the characteristics of targeted killing tumor cells and specific silencing STAT3 expression. It shows good biocompatibility to the organs and allows continuous controlled release of chemotherapy drugs. The drug release behavior has typical pH sensitivity, and the release rate is higher in acidic environment than in neutral environment. The VCPH NPs can up-regulate the expression of PTEN protein. The activity of PTEN lipid phosphatase can dephosphorylate phosphatidylinositol triphosphate (PIP3) into phosphatidylinositol diphosphate and inactivate it, and then inhibit the Pl3K/AKT pathway, resulting in the death of neighboring tumor cells. In addition, VCPH NPs can also down-regulate the expression of CD31 protein, thereby reducing the occurrence of angiogenesis and further reducing the survival rate of tumor cells. The expression of STAT3 is significantly down-regulated by VCPH NPs, which can further improve the drug sensitivity while killing tumors. The construction and development of this dual-loaded cooperative delivery system provides important implications for the combined treatment of tumors, and provides an effective way for the precise targeted treatment of NSCLC.

Ethics approval and consent to participate

All animals were kept under a 12 h light-dark cycles at consistent temperature (25 ± 3 °C) and relative humidity (60–70 %). Experiments were performed in accordance with the ethical guidelines of the Experimental Animal Management Committee of Ocean University of China and were in complete compliance with the National Institutes of Health Guide for the Care and Use of Laboratory Animals.

CRediT authorship contribution statement

Le Sun: Writing – original draft, Validation, Methodology, Formal analysis. **Jishang Sun:** Writing – original draft, Validation, Methodology, Formal analysis. **Cuiyao Li:** Formal analysis, Validation. **Keying**

Wu: Data curation, Formal analysis, Software. **Zhiyang Gu:** Investigation. **Lan Guo:** Validation. **Yi Zhou:** Methodology. **Baoqin Han:** Supervision. **Jing Chang:** Writing – review & editing, Supervision, Resources, Project administration, Conceptualization.

Declaration of competing interest

The authors declare that they have no known competing financial interests or personal relationships that could have appeared to influence the work reported in this paper.

Acknowledgement

The authors wish to thank Shandong Provincial Key Research and Development Program (Major Scientific and Technological Innovation Project, No. 2022CXGC010505), National Natural Science Foundation of China (No. 51773188), National Key Research and Development Program of China (No. 2023YFC2812004), Key Project of Natural Science Foundation of Shandong Province (No. ZR2020KE016).

References

[1] J.E. Hart, Air pollution affects lung cancer survival, Thorax 71 (2016) 875–876. http://10.1136/thoraxjnl-2016-208967.
[2] X. Zhao, Y. Cao, R. Lu, Z. Zhou, C. Huang, L. Li, J. Huang, R. Chen, Y. Wang, J. Huang, J. Cheng, J. Zheng, Y. Fu, J. Yu, Phosphorylation of AGO2 by TBK1 promotes the formation of oncogenic miRISC in NSCLC, Adv. Sci. 11 (2024). http://10.1002/advs.202305541.
[3] J.C. Ho, C. Leung, Management of co-existent tuberculosis and lung cancer, Lung Cancer 122 (2018) 83–87. http://10.1016/j.lungcan.2018.05.030.
[4] C. Cheng, P. Wang, Y. Yang, X. Du, H. Xia, J. Liu, L. Lu, H. Wu, Q. Liu, Smoking-induced M2-TAMs, via circEML4 in EVs, promote the progression of NSCLC through ALKBH5-regulated m6A modification of SOCS2 in NSCLC cells, Adv. Sci. 10 (2023). http://10.1002/advs.202300953.
[5] B. Xu, F. Zeng, J. Deng, L. Yao, S. Liu, H. Hou, Y. Huang, H. Zhu, S. Wu, Q. Li, W. Zhan, H. Qiu, H. Wang, Y. Li, X. Yang, Z. Cao, Y. Zhang, H. Zhou, A homologous and molecular dual-targeted biomimetic nanocarrier for EGFR-related non-small cell lung cancer therapy, Bioact. Mater. 27 (2023) 337–347. http://10.1016/j.bioactmat.2023.04.005.
[6] F. Gao, X. Yang, X. Luo, X. Xue, C. Qian, M. Sun, Photoactivated nanosheets accelerate nucleus access of cisplatin for drug-resistant cancer therapy, Adv. Funct. Mater. 30 (2020). http://10.1002/adfm.202001546.
[7] T.G. Phan, P.I. Croucher, The dormant cancer cell life cycle, Nat. Rev. Cancer 20 (2020) 398–411. http://10.1038/s41568-020-0263-0.
[8] Y.G. Assaraf, A. Brozovic, A.C. Gonçalves, D. Jurkovicova, A. Linē, M. Machuqueiro, S. Saponara, A.B. Sarmento-Ribeiro, C.P.R. Xavier, M. H. Vasconcelos, The multi-factorial nature of clinical multidrug resistance in cancer, Drug Resist, Update 46 (2019) 100645. http://10.1016/j.drup.2019.100645.
[9] C. He, L. Yu, L. Ding, Y. Chen, Y. Hao, Self-assembled/drug-composed nanomedicine for synergistic photonic hyperthermia and targeted therapy of breast cancer by inhibiting ERK, AKT, and STAT3 signaling cascades, Adv. Funct. Mater. 30 (2020) 1908907. http://10.1002/adfm.201908907.
[10] X. Sun, P. Zhao, J. Lin, K. Chen, J. Shen, Recent advances in access to overcome cancer drug resistance by nanocarrier drug delivery system, Cancer Drug Resist. 6 (2023) 390–415. http://10.20517/cdr.2023.16.
[11] Q. Deng, B. Xie, L. Wu, X. Ji, C. Li, L. Feng, Q. Fang, Y. Bao, J. Li, S. Jin, C. Ding, Y. Li, S. Zhou, Competitive evolution of NSCLC tumor clones and the drug resistance mechanism of first-generation EGFR-TKIs in Chinese NSCLC patients, Heliyon 4 (2018) e01031. http://10.1016/j.heliyon.2018.e01031.
[12] Y. Kong, D. Shuangshuang, X. Liang, X. Zhou, RPS9 promotes the progression of NSCLC via activation Stat3 and Erk signaling pathways, J. Cancer 13 (2022) 1346–1355. http://10.7150/jca.67513.
[13] J. Zhao, Y. Qi, Y. Yu, STAT3: a key regulator in liver fibrosis, Ann. Hepatol. 21 (2021) 100224. http://10.1016/j.aohep.2020.06.010.
[14] M. Zhou, P. Zhang, M. Da, R. Yang, Y. Ma, J. Zhao, T. Ma, J. Xia, G. Shen, Y. Chen, D. Chen, A pan-cancer analysis of the expression of STAT family genes in tumors and their relationship to the tumor microenvironment, Front. Oncol. 12 (2022) 925537. http://10.3389/fonc.2022.925537.
[15] I. Chaib, N. Karachaliou, S. Pilotto, S.J. Codony, X. Cai, X. Li, A. Drozdowskyj, C. C. Servat, J. Yang, C. Hu, A.F. Cardona, G.L. Vivanco, A. Vergnenegre, J. M. Sanchez, M. Provencio, F. de Marinis, A. Passaro, E. Carcereny, N. Reguart, C. G. Campelo, C. Teixido, I. Sperduti, S. Rodriguez, C. Lazzari, A. Verlicchi, I. de Aguirre, C. Queralt, J. Wei, R. Estrada, D.L.B.R. Puig, J.L. Ramirez, K. Jacobson, H. J. Ditzel, M. Santarpia, S. Viteri, M.A. Molina, C. Zhou, P. Cao, P.C. Ma, T. G. Bivona, R. Rosell, Co-Activation of STAT3 and YES-associated protein 1 (YAP1) pathway in EGFR-mutant NSCLC, JNCI-J. Natl. Cancer Inst. 109 (2017). http://10.1093/jnci/djx014.
[16] X. Xu, D. Li, J. Liu, Z. Ma, H. Huang, L. Min, L. Dai, S. Dong, Downregulation of PTPRK promotes cell proliferation and metastasis of NSCLC by enhancing STAT3 activation, Anal. Cell Pathol. 2019 (2019) 1–7. http://10.1155/2019/4265040.
[17] M. Rammohan, R.S. Bhansali, Y. Tsai, A. Dong, S. Malinge, J. Bourquin, J. D. Crispino, STAT3 is activated by DYRK1A and is a potential therapeutic target in B-ALL, Blood 132 (2018) 3898. http://10.1182/blood-2018-99-115429.
[18] L. Lu, F. Zhu, M. Zhang, Y. Li, A.C. Drennan, S. Kimpara, I. Rumball, C. Selzer, H. Cameron, A. Kellicut, A. Kelm, F. Wang, T.A. Waldmann, L. Rui, Gene regulation and suppression of type I interferon signaling by STAT3 in diffuse large B cell lymphoma, Proc. Natl. Acad. Sci. USA 115 (2018). http://10.1073/pnas.1715118115.
[19] X. Song, W. Tang, H. Peng, X. Qi, J. Li, FGFR leads to sustained activation of STAT3 to mediate resistance to EGFR-TKIs treatment, Invest. N. Drugs 39 (2021) 1201–1212. http://10.1007/s10637-021-01061-1.
[20] H. Wang, S. Si, M. Jiang, L. Chen, K. Huang, W. Yu, Leukemia inhibitory factor is involved in the pathogenesis of NSCLC through activation of the STAT3 signaling pathway, Oncol. Lett. 22 (2021) 1. http://10.3892/ol.2021.12924.
[21] K.A. Papavassiliou, G. Marinos, A.G. Papavassiliou, Combining STAT3-targeting agents with immune checkpoint inhibitors in NSCLC, Cancers 15 (2023) 386. http://10.3390/cancers15020386.
[22] Z. Zhao, C. Li, Y. Zhang, C. Li, Y. Chu, X. Li, P. Liu, H. Chen, Y. Wang, B. Su, Q. Chen, T. Sun, C. Jiang, Nanomaterials with dual immunomodulatory functions for synergistic therapy of breast cancer brain metastases, Bioact. Mater. 27 (2023) 474–487. http://10.1016/j.bioactmat.2023.04.021.
[23] L.F. Gao, L.J. Wen, H. Yu, L. Zhang, Y. Meng, Y.T. Shao, D.Q. Xu, X.J. Zhao, Knockdown of Stat3 expression using RNAi inhibits growth of laryngeal tumors in vivo, Acta Pharmacol. Sin. 27 (2006) 347–352. http://10.1111/j.1745-7254.2006.00277.x.
[24] Y.P. Ma, Y. Yang, S. Zhang, X. Chen, N. Zhang, W. Wang, Z.X. Cao, Y. Jiang, X. Zhao, Y.Q. Wei, H.X. Deng, Efficient inhibition of lung cancer in murine model by plasmid-encoding VEGF short hairpin RNA in combination with low-dose DDP, J. Exp. Clin. Cancer Res. 29 (2010) 56. http://10.1186/1756-9966-29-56.
[25] D. Zhang, Y. Sun, S. Wang, Y. Zou, M. Zheng, B. Shi, Brain-targeting metastatic tumor cell membrane cloaked biomimetic nanomedicines mediate potent chemodynamic and RNAi combinational therapy of glioblastoma, Adv. Funct. Mater. 32 (2022). http://10.1002/adfm.202209239.
[26] M. Zhang, X. Qin, Y. Gao, J. Liang, D. Xiao, X. Zhang, M. Zhou, Y. Lin, Transcutaneous immunotherapy for RNAi: a cascade-responsive decomposable nanocomplex based on polyphenol-mediated framework nucleic acid in psoriasis, Adv. Sci. 10 (2023) e2303706. http://10.1002/advs.202303706.
[27] H. Kim, J. Jeong, D. Kim, G. Kwak, S.H. Kim, J.B. Lee, Bubbled RNA-based cargo for boosting RNA interference, Adv. Sci. 4 (2017). http://10.1002/advs.201600523.
[28] X. Zhu, T. Li, Y. Dang, Y. Feng, P. Huang, A novel in vitro transcription method for producing siRNAs without specific sequence requirements, Mol. Biotechnol. 31 (2005) 187–192. http://10.1385/MB:31:3:187.
[29] P. Svoboda, Key mechanistic principles and considerations concerning RNA interference, Front. Plant Sci. 11 (2020) 1237. http://10.3389/fpls.2020.01237.
[30] Y. Zhang, L. Yang, H. Wang, J. Huang, Y. Lin, S. Chen, X. Guan, M. Yi, S. Li, L. Zhang, Bioinspired metal–organic frameworks mediated efficient delivery of siRNA for cancer therapy, Chem. Eng. J. 426 (2021) 131926. http://10.1016/j.cej.2021.131926.
[31] P. Sheng, K.A. Flood, M. Xie, Short hairpin RNAs for strand-specific small interfering RNA production, Front. Bioeng. Biotechnol. 8 (2020) 940. http://10.3389/fbioe.2020.00940.
[32] G.P. Bai, G.H. Yan, G.J. Wang, P. Wan, X.F. Liu, H. Wang, R.H. Zhang, Effects of lentiviral vector-mediated shRNA silencing of TGFbeta1 on the expression of Col1a1 in rat hepatic stellate cells, Mol. Med. Rep. 16 (2017) 2785–2790. http://10.3892/mmr.2017.6945.
[33] A. Alagia, R. Eritja, siRNA and RNAi optimization, Wiley Interdiscip. Rev. RNA. 7 (2016) 316–329. http://10.1002/wrna.1337.
[34] J.W. Lee, J. Choi, Y. Choi, K. Kim, Y. Yang, S.H. Kim, H.Y. Yoon, I.C. Kwon, Molecularly engineered siRNA conjugates for tumor-targeted RNAi therapy, J. Contr. Release 351 (2022) 713–726. http://10.1016/j.jconrel.2022.09.040.
[35] S. Pan, Y. Deng, J. Fu, Y. Zhang, Z. Zhang, X. Ru, X. Qin, TRIM52 promotes colorectal cancer cell proliferation through the STAT3 signaling, Cancer Cell Int. 19 (2019). http://10.1186/s12935-019-0775-4.
[36] R. Raguraman, S. Shanmugarama, M. Mehta, J. Elle Peterson, Y.D. Zhao, A. Munshi, R. Ramesh, Drug delivery approaches for HuR-targeted therapy for lung cancer, Adv. Drug Deliv. Rev. 180 (2022) 114068, https://doi.org/10.1016/j.addr.2021.114068.
[37] C.Y.X. Chua, J. Ho, A. Susnjar, G. Lolli, N. Di Trani, F. Pesaresi, M. Zhang, E. Nance, A. Grattoni, Intratumoral nanofluidic system for enhancing tumor biodistribution of agonist CD40 antibody, Adv. Ther. 3 (2020). http://10.1002/adtp.202000055.
[38] Y. Sakurai, H. Hatakeyama, Y. Sato, M. Hyodo, H. Akita, H. Harashima, Gene silencing via RNAi and siRNA quantification in tumor tissue using MEND, a liposomal siRNA delivery system, Mol. Ther. 21 (2013) 1195–1203. http://10.1038/mt.2013.57.
[39] P. Yuan, T. Yang, T. Liu, X. Yu, Y. Bai, Y. Zhang, X. Chen, Nanocomposite hydrogel with NIR/magnet/enzyme multiple responsiveness to accurately manipulate local drugs for on-demand tumor therapy, Biomaterials 262 (2020) 120357. http://10.1016/j.biomaterials.2020.120357.
[40] X. Zhou, X. He, K. Shi, L. Yuan, Y. Yang, Q. Liu, Y. Ming, C. Yi, Z. Qian, Injectable thermosensitive hydrogel containing erlotinib-loaded hollow mesoporous silica nanoparticles as a localized drug delivery system for NSCLC therapy, Adv. Sci. 7 (2020). http://10.1002/advs.202001442.

[41] F. Boateng, W. Ngwa, Delivery of nanoparticle-based radiosensitizers for radiotherapy applications, Int. J. Mol. Sci. 21 (2019) 273. http://10.3390/ijms21010273.
[42] H. Chu, R. Sun, J. Sheng, X. Li, X. Li, W. Wang, L. Teng, W. Zhu, Polymeric prodrug by supramolecular polymerization, React. Funct. Polym. 191 (2023) 105654. http://10.1016/j.reactfunctpolym.2023.105654.
[43] L. Ruan, J. Chen, C. Du, H. Lu, J. Zhang, X. Cai, R. Dou, W. Lin, Z. Chai, G. Nie, Y. Hu, Mitochondrial temperature-responsive drug delivery reverses drug resistance in lung cancer, Bioact. Mater. 13 (2022) 191–199. http://10.1016/j.bioactmat.2021.10.045.
[44] S. Li, C. Meng, Q. Hao, L. Dai, J. Shi, J. Xu, X. Zhou, S. Zhao, J. Yang, H. Kang, Y. Hou, M. Zhang, X. Ma, M. Tan, H. Wu, A multistage-responsive antibody-delivery strategy to improve immunotherapy for NSCLC brain metastasis by ultrasensitive releasing and tumor-anchoring, Adv. Funct. Mater. 34 (2024) 2312595, https://doi.org/10.1002/adfm.202312595.
[45] K. Li, D. Li, L. Zhao, Y. Chang, Y. Zhang, Y. Cui, Z. Zhang, Calcium-mineralized polypeptide nanoparticle for intracellular drug delivery in osteosarcoma chemotherapy, Bioact. Mater. 5 (2020) 721–731. http://10.1016/j.bioactmat.2020.04.010.
[46] X. Liu, J. Sun, J. Gu, L. Weng, X. Wang, L. Zhu, Q. Luo, Z. Chen, Effective drug and shRNA delivery for synergistic treatment of triple-negative breast cancer by sequentially targeting tumor hypoxia, Chem. Eng. J. 470 (2023) 144271. http://10.1016/j.cej.2023.144271.
[47] C. Chen, M. Shen, X. Wan, L. Sheng, Y. He, M. Xu, M. Yuan, Z. Ji, J. Zhang, Activated T cell-derived exosomes for targeted delivery of AXL-siRNA loaded paclitaxel-poly-L-lysine prodrug to overcome drug resistance in triple-negative breast cancer, Chem. Eng. J. 468 (2023) 143454. http://10.1016/j.cej.2023.143454.
[48] S. Peers, A. Montembault, C. Ladavière, Chitosan hydrogels for sustained drug delivery, J. Contr. Release 326 (2020) 150–163. http://10.1016/j.jconrel.2020.06.012.
[49] R. Parhi, Drug delivery applications of chitin and chitosan: a review, Environ. Chem. Lett. 18 (2020) 577–594. http://10.1007/s10311-020-00963-5.
[50] A. Ali, S. Ahmed, A review on chitosan and its nanocomposites in drug delivery, Int. J. Biol. Macromol. 109 (2018) 273–286. http://10.1016/j.ijbiomac.2017.12.078.
[51] I.P.D. Picola, Q. Shi, J.C. Fernandes, M.S. Petrônio, A.M.F. Lima, V.A. de Oliveira Tiera, M.J. Tiera, Chitosan derivatives for gene transfer: effect of phosphorylcholine and diethylaminoethyl grafts on the in vitro transfection efficiency, J. Biomater. Sci. Polym. Ed. 27 (2016) 1611–1630. http://10.1080/09205063.2016.1225333.
[52] J. Chang, X. Xu, H. Li, Y. Jian, G. Wang, B. He, Z. Gu, Components simulation of viral envelope via amino acid modified chitosans for efficient nucleic acid delivery: in vitro and in vivo study, Adv. Funct. Mater. 23 (2013) 2691–2699. http://10.1002/adfm.201202503.
[53] X. Chen, L. Guo, S. Ma, J. Sun, C. Li, Z. Gu, W. Li, L. Guo, L. Wang, B. Han, J. Chang, Construction of multi-program responsive vitamin E succinate-chitosan-histidine nanocarrier and its response strategy in tumor therapy, Int. J. Biol. Macromol. 246 (2023) 125678. http://10.1016/j.ijbiomac.2023.125678.
[54] X. Chen, J. Gu, L. Sun, W. Li, L. Guo, Z. Gu, L. Wang, Y. Zhang, W. Zhang, B. Han, J. Chang, Efficient drug delivery and anticancer effect of micelles based on vitamin E succinate and chitosan derivatives, Bioact. Mater. 6 (2021) 3025–3035. http://10.1016/j.bioactmat.2021.02.028.